Petit-spot lavas on the western Pacific Plate: contribution of carbonatite and recycled oceanic crust

Kazuto Mikuni[1,2]*, Naoto Hirano[2,3], Shiki Machida[4], Hirochika Sumino[5], Norikatsu Akizawa[6], Akihiro Tamura[7], Tomoaki Morishita[7], Yasuhiro Kato[4,8,9]

[1] AIST, Geological Survey of Japan, Research Institute of Geology and Geoinformation, Central 7, 1-1-1, Higashi, Tsukuba, Ibaraki 305-8567, Japan.

[2] Graduate School of Science, Tohoku University, 6-3 Aramaki-Aoba, Aoba-ku, Sendai 980–8578, Japan.

[3] Center for Northeast Asian Studies, Tohoku University, 41 Kawauchi, Aoba-ku, Sendai 980–8576, Japan.

[4] Ocean Resources Research Center for Next Generation, Chiba Institution of Technology, 2-17-1 Tsudanuma, Narashino 275-0016, Japan.

[5] Research Center for Advanced Science and Technology, the University of Tokyo, 4-6-1 Komaba, Meguro-ku, Tokyo 153-8904, Japan

[6] Atmosphere and Ocean Research Institute, the University of Tokyo, 5-1-5, Kashiwanoha, Kashiwa 277-8564, Japan.

[7] Earth Science Course, Kanazawa University, Kakuma, Kanazawa 920-1192, Japan.

[8] Department of Systems Innovation, School of Engineering, The University of Tokyo, 7-3-1 Hongo, Bunkyo-ku, Tokyo 113-8656, Japan.

[9] Submarine Resources Research Center, Research Institute for Marine Resources Utilization, Japan Agency for Marine-Earth Science and Technology (JAMSTEC), 2-15 Natsushima-cho, Yokosuka, Kanagawa, 237-0061, Japan.

* *Correspondence to* Kazuto Mikuni (kazuto.mikuni @aist.go.jp)

Authors' e-mail addresses and ORCiD numbers

Kazuto Mikuni[1,2]*	kazuto.mikuni@aist.go.jp	0000-0001-6939-4333
Naoto Hirano[2,3]	nhirano@tohoku.ac.jp	0000-0003-0980-3929
Shiki Machida[4]	shiki.machida@p.chibakoudai.jp	0000-0002-1069-7214
Hirochika Sumino[5]	sumino@igcl.c.u-tokyo.ac.jp	0000-0002-4689-6231
Norikatsu Akizawa[6]	akizawa@g.ecc.u-tokyo.ac.jp	0000-0003-4210-1160
Akihiro Tamura[7]	aking826@gmail.com	0000-0002-9112-7976
Tomoaki Morishita[7]	moripta@gmail.com	0000-0002-8724-6868
Yasuhiro Kato[4,8,9]	ykato@sys.t.u-tokyo.ac.jp	0000-0002-5711-8304

The manuscript is going to be submitted to *Solid Earth*.

Keywords: Petit-spot volcano, alkali basalt, carbonatite, asthenosphere

41   **Abstract**

43   Petit-spot volcanism, which occurs owing to the plate flexure, have been reported from around
44   the world. As the petit-spot melts ascent from the asthenosphere, they provide the essential information
45   of the lithosphere–asthenosphere boundary (LAB). Here, we observed the lava outcrops of six
46   monogenetic volcanoes formed by petit-spot volcanism in the western Pacific. Thereafter, we
47   determined the $^{40}Ar/^{39}Ar$ ages, major and trace element compositions, and Sr, Nd, and Pb isotopic
48   ratios of the petit-spot basalts. The $^{40}Ar/^{39}Ar$ ages of two monogenetic volcanoes were ca. 2.6 Ma
49   (million years ago) and ca. 0 Ma, respectively. The isotopic compositions of the western Pacific petit-
50   spot basalts suggest geochemically similar melting sources. They were likely derived from a mixture
51   of high-μ (HIMU) mantle-like and enriched mantle (EM)-1-like components related to
52   carbonatitic/carbonated materials and recycled crustal components. A mass balance-based melting
53   model implied that the characteristic trace element composition (i.e., Zr, Hf, and Ti depletions) of the
54   western Pacific petit-spot magmas could be explained by the partial melting of ~5% crust-bearing
55   garnet lherzolite with 10% carbonatite flux to a given mass of the source. This result confirms the
56   involvement of carbonatite melt and recycled crust in the source of petit-spot melts and provides an
57   implication for the genesis of tectonic-induced volcanoes including Hawaiian North Arch volcanics
58   and Samoan petit-spot like rejuvenated volcanoes having similar trace element composition to petit-
59   spot basalts.

60

61

62   **Short Summary**

63

64   Plate tectonics theory is understood as the motion of rocky plate (lithosphere) over ductile zone
65   (asthenosphere). The causes of lithosphere–asthenosphere boundary (LAB) is controversial, but petit-
66   spot volcanism supports the presence of melt at the LAB. We conducted geochemistry, geochronology,
67   and geochemical modeling for petit-spot volcanoes on the western Pacific Plate, and the results
68   suggested that carbonatite melt and recycled oceanic crust have induced the partial melting at the LAB.

69

70   **1 Introduction**

71

72   Among the upper mantle-derived alkali basaltic lavas in oceanic settings, those on thicker plates
73   away from the mid-ocean ridge, could be divided into plume-related and non-plume-related volcanoes.
74   For example, plume-related North Arch and post-erosional (rejuvenated-stage) volcanoes have been
75   reported in Hawaii and Samoa (Bianco et al., 2005; Bizimis et al., 2013; Clague and Frey, 1982; Clague

76 and Moore, 2002; Dixon et al., 2008; Frey et al., 2000; Garcia et al., 2016; Hart et al., 2004; Konter

77 and Jackson, 2012; Koppers et al., 2008; Reinhard et al., 2019; Yang et al., 2003). Non-plume related

78 intraoceanic alkali volcanoes, called as petit-spot volcanoes, probably originate where nearby plate

79 subduction causes plate flexures and upwelling of asthenospheric magma (Hirano et al., 2006; Hirano

80 and Machida, 2022; Machida et al., 2015, 2017; Yamamoto et al., 2014, 2018, 2020). Therefore, the

81 occurrence of petit-spot volcanisms supports the presence of melt at lithosphere–asthenosphere

82 boundary (LAB) below the area at least.

83 The presence of melt in the uppermost asthenosphere could be due to small-scale convection,

84 heating, or the presence of hydrous or carbonatitic components (Hua et al., 2023; Korenaga, 2020). In

85 particular, the presence of CO_2 and carbonated/carbonatitic materials is key in the formation of alkaline,

86 silica-undersaturated melt in the upper mantle (Dasgupta and Hirschmann, 2006; Dasgupta et al., 2007,

87 2013; Kiseeva et al., 2013; Novella et al., 2014). Experimental studies have shown that the solidus of

88 carbonate-bearing peridotite is lower than that of CO_2-free peridotite (Falloon and Green, 1989. 1990;

89 Foley et al., 2009; Ghosh et al., 2009). In addition, carbonatites and Si-undersaturated melts are

90 generated through the partial melting of CO_2-bearing or carbonated peridotite. The produced melts

91 could exhibit continuous chemical variations depending on pressure (i.e., depth). Namely, carbonatitic

92 melts are produced in the deep asthenosphere (300 km to 110 km), while carbonated or alkali silicate

93 melts are generated in the shallower upper mantle (~110 km to ~75 or 60 km) (Keshav and

94 Gudfinnsson, 2013; Massuyeau et al., 2015, 2021). Indeed, primary carbonated silicate magma and

95 evolved alkali basalts have been simultaneously observed at the post-spreading ridge in the South

96 China Sea (Zhang et al., 2017; Zhong et al., 2021). Hawaiian rejuvenated volcanoes were also

97 attributed to be explained by a carbonatite-metasomatized source with or without silicate

98 metasomatism (Borisova and Tilhac, 2021; Dixon et al., 2008; Zhang et al., 2022).

99 Submarine petit-spot volcanoes on the subducting northwestern (NW) Pacific Plate may

100 originate from carbonate-bearing materials and crustal components (pyroxenite/eclogite) based on the

101 characteristic trace element, enriched mantle (EM)-1-like Sr, Nd, and Pb isotopic, and relatively low

102 Mg isotopic compositions (Liu et al., 2020; Machida et al., 2009, 2015). In particular, the depletion of

103 specific high-field-strength elements (HFSEs) (i.e., Zr, Hf, and Ti) and the abundant CO_2 of petit-spot

104 basalts imply that their melting sources are related to carbonated materials (Hirano and Machida, 2022;

105 Okumura and Hirano, 2013). Here, the nature of the uppermost part of the asthenosphere beneath the

106 oldest Pacific Plate aged 160 Ma, was characterized using the eruptive ages and geochemical

107 properties of six newly observed petit-spot volcanoes and lava outcrops. We verified the contribution

108 of carbonatitic components and crustal materials to the melting source of petit-spot volcanoes to

109 understand the nature of the underlying lithosphere-asthenosphere system and model the geodynamic

110 evolution of the region.

111

2 Background

In the last 20 years, the increasing knowledge of petit-spot volcanic settings has provided useful insights on the nature of the lithosphere-asthenosphere system, especially in the NW Pacific region (Hirano et al., 2006; Hirano and Machida, 2022). As other implications, subducted petit-spot volcanic fields with geological disturbances on the seafloor play a role in controlling the hypocentral regions of megathrust earthquakes (Fujiwara et al., 2007; Fujie et al., 2020; Akizawa et al., 2022), and the vestige of hydrothermal activity owing to petit-spot magmatism were recently reported (Azami et al., 2023).

Petit-spot melts, which originated from the asthenosphere unrelated to mantle plume, could be a key to elucidating the nature of the LAB (Hirano and Machida, 2022). Their asthenospheric origin was supported by MORB-like noble gas isotopic ratios, multi-phase saturation experiment, and geochemistry (Hirano et al., 2006; Hirano and Machida, 2022; Machida et al., 2015, 2017; Yamamoto et al., 2018). The LAB is identified as a discontinuous transition in seismic velocities at the base of the lithosphere, and its causes are attributed to hydration, melting, and mineral anisotropy with considerations for the unique characteristics in each tectonic setting (e.g., Rychert and Shearer, 2009). The occurrence of petit-spot volcanism substantiates the existence of melt at the LAB below the area at least (Hirano et al., 2006). Recently, similar volcanic activities have been observed worldwide including Java (Sunda) Trench, Tonga Trench, Chile Trench, Mariana Trench, Costa Rica, North American Basin and Range, and southern offshore of Greenland, implying the universal occurrence of petit-spot and similar magmatisms (Axen et al., 2018; Buchs et al., 2013; Falloon et al., 2022; Hirano et al., 2013, 2016, 2019; Reinhard et al., 2019; Taneja et al., 2016; Uenzelmann-Neben et al., 2012; Yamamoto et al., 2018, 2020; Zhang et al., 2019). Although there is still an open question of whether the LAB discontinuity is due to the differences in the physical properties of minerals (e.g., Hirth and Kohlstedt, 1996; Kang and Karato, 2023; Karato and Jung, 1998; Katsura and Fei, 2021; Stixrude and Lithgow-Bertelloni, 2005; Wang et al., 2006) or the presence of partial melts (e.g., Audhkhasi and Singh, 2022; Chantel et al., 2016; Conrad et al., 2011; Debayle et al., 2020; Herath et al., 2022; Hua et al., 2023; Kawakatsu et al., 2009; Mierdel et al., 2007; Sakamaki et al., 2013; Yoshino et al., 2006), the occurrence of petit-spot volcanism reveals the partial melting of the asthenospheric mantle of the region because they erupted on the seafloor without hotspot and ridge activities (Hirano et al., 2006; Hirano and Machida, 2022; Machida et al., 2015, 2017; Yamamoto et al., 2014, 2018, 2020).

The petit-spot volcanic province on the abyssal plain of the western Pacific is surrounded by Cretaceous seamounts and oceanic islands of the Western Pacific Seamount Province (Koppers et al., 2003) and located approximately 100 km southeast of the Minamitorishima (Marcus) Island (Fig. 1a). The study area corresponds to the oldest portion of the Pacific Plate aged at 160 Ma and the foot of

148 the outer-rise bulge related to the Mariana subduction system (Hirano et al., 2019; Fig. 1b). Such a

149 subduction-related fore-bulge in front of the Mariana Trench has been numerically modeled and

150 detected in satellite gravity maps despite crosscutting by several seamounts (Bellas et al., 2022; Hirano

151 et al., 2019; Zhang et al., 2014, 2020). The petrography, geochemistry, and geochronology of petit-

152 spot basalts and zircons in peperites, which were collected from a knoll, suggested that petit-spot

153 magmas in this region ascend from the asthenosphere along the concavely flexed plate in response to

154 subduction into the Mariana Trench at younger than ~3 Ma (Yamamoto et al., 2018; Hirano et al.,

155 2019). Below the study area, low seismic velocity zone is observed under the lithosphere (Li et al.,

156 2019; Fig. 1c). Notwithstanding the low velocity anomalies crosscutting the lower mantle (Fig. 1c),

157 no active hotspots (i.e., heat supplies) have been reported around the western Pacific petit-spot

158 province surrounded by Cretaceous Wake seamount chains including Minamitorishima Island and

159 Paleogene intraplate volcanoes (Koppers et al., 2003; Aftabuzzaman et al., 2021; Hirano et al., 2021).

160 The other petit-spot lava outcrops were observed in a volcanic cluster during three research cruises

161 using the research vessel (RV) *Yokosuka* (YK16-01, YK18-08, and YK19-05S) with five dives using

162 the submersible, *Shinkai* 6500 (6K#1466, 6K#1521, 6K#1522, 6K#1542, and 6K#1544; Fig. 2), and

163 fresh basalts were collected. The information of sampling point, depth, thickness of palagonite rind

164 and manganese-crust, and age of the western Pacific petit-spot basalts are provided in Table 1.

165
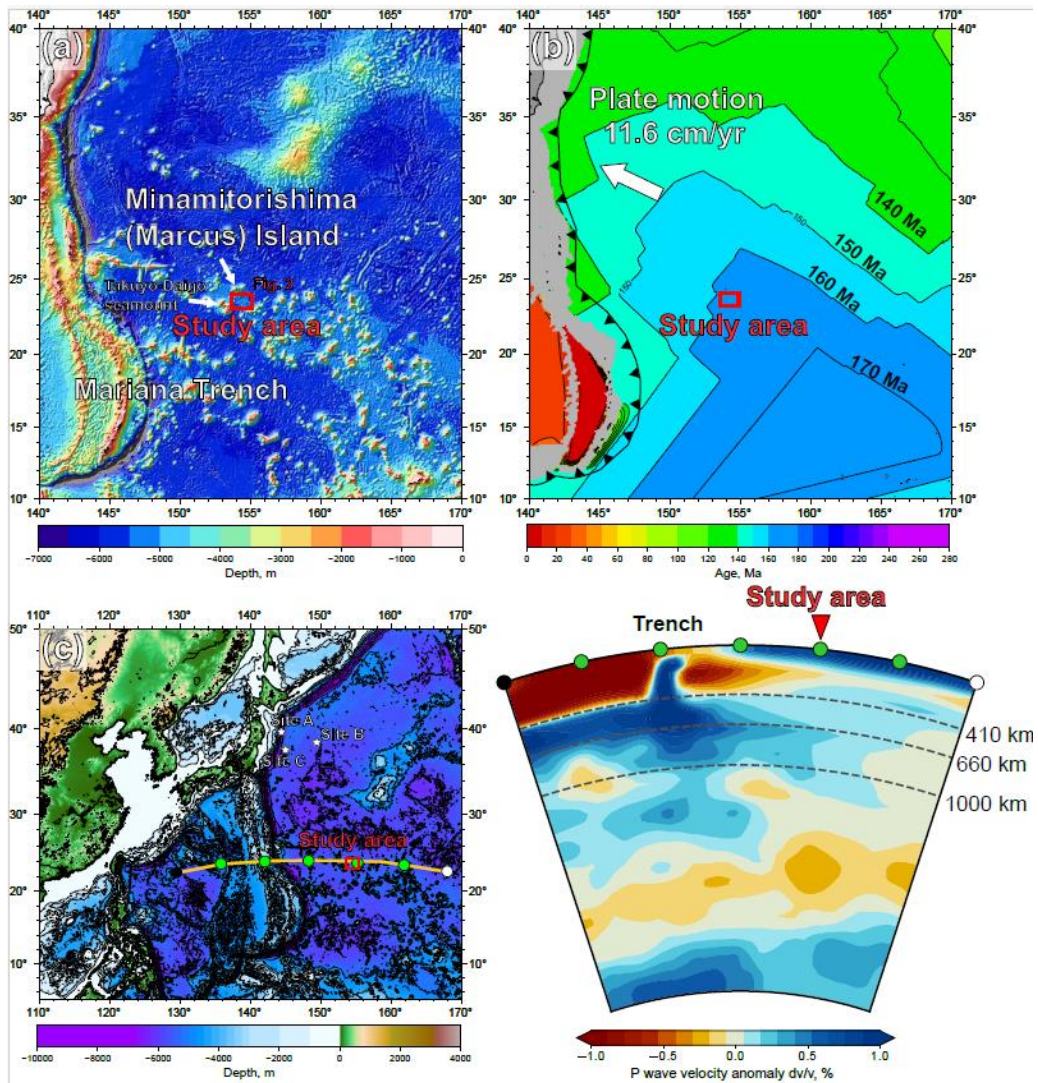
166   Fig. 1. Geological and geophysical information of the study area. (a) Bathymetry of the western Pacific near the

167   Mariana Trench. The red box shows the study area to the southeast of Minamitorishima (Marcus) Island

168   (Fig. 2). The bathymetric data are adopted from ETOPO1 (NOAA National Geophysical Data Center;

169   http://www.ngdc.noaa.gov/). (b) Seafloor age map of the same area as (a). This study area is on a 160–

170   170 Ma Pacific Plate, called the Jurassic Quiet Zone (JQZ) (Tivey et al. 2006). The present absolute

171   motion of the Pacific Plate and the seafloor age are derived from studies by Gripp and Gordon (1990)

172   and Müller et al. (2008), respectively. (c) The cross-section P-wave tomography beneath the thick

173   yellow line including the study area on the ETOPO1 bathymetry map (left). The tomographic image

174   (right) was drawn using the SubMachine (Hosseini et al., 2018;

175   http://www.earth.ox.ac.uk/~smachine/cgi/index.php) on applying the data of Lu et al. (2019).

Table. 1
Information of the collected western Pacific petit-spot basalts

Cruise	Dive	Sample name	Latitude (N)	Longitude (E)	Depth, m	Palagonite rind, mm [*1]	Manganese crust, mm [*1]	Ar-Ar age, Ma
YK16-01	6K#1466	R3-001	23° 19.1009	154° 15.0950	5453	4.45	7.155	
		R3-04	23° 19.1009	154° 15.0950	5453	3.005	5.805	
		R6-001	23° 19.4475	154° 15.0367	5300	6.61	5.205	2.56±0.34
		R7-001	23° 19.4713	154° 15.0000	5267	5.54	4.31	
		R7-003	23° 19.4713	154° 15.0000	5267	-	–	
YK18-08	6K#1521	R04	23° 5.0880	154° 23.7360	5546	1.045	5.935	
		R05	23° 5.0880	154° 23.7360	5546	-	5.625	
	6K#1522	R01	23° 27.6420	153° 58.3140	5300	6.015	5.78	-0.11±0.23 [*2]
		R02	23° 27.6420	153° 58.3140	5300	4.505	2.66	
		R03	23° 27.6420	153° 58.3140	5300	5.44	4.04	
		R05	23° 27.6360	153° 58.3080	5294	2.92	4.785	
		R12	23° 27.4920	153° 58.0620	5189	6.05	5.56	
		R13	23° 27.4920	153° 58.0620	5189	4.545	5.895	
		R14	23° 27.3540	153° 57.8160	5303	2.04	5.475	
		R16	23° 27.4680	153° 57.1200	5182	3.825	3.845	
		R17	23° 27.4680	153° 57.1200	5182	5.19	5.67	
YK19-05S	6K#1542	R03	23° 44.1926	154° 45.6900	5359	3.43	4.26	
		R05	23° 44.1926	154° 45.6900	5359	3.245	4.355	
		R06	23° 44.7064	154° 44.1200	5190	-	-	
		R09	23° 44.7064	154° 44.1200	5190	-	-	
	6K#1544	R04	23° 43.9555	154° 49.4277	5488	4.39	4.955	
		R05	23° 43.9555	154° 49.4277	5488	2.965	4.97	
		R06	23° 43.9555	154° 49.4277	5488	3.425	5.82	

＊1: The samples which have no data of palagonite and/or Mn-crust thickness are due to the lack of them or crumbled.

＊2: This is a reference value due to the lack of radiogenic ^{40}Ar in this sample.
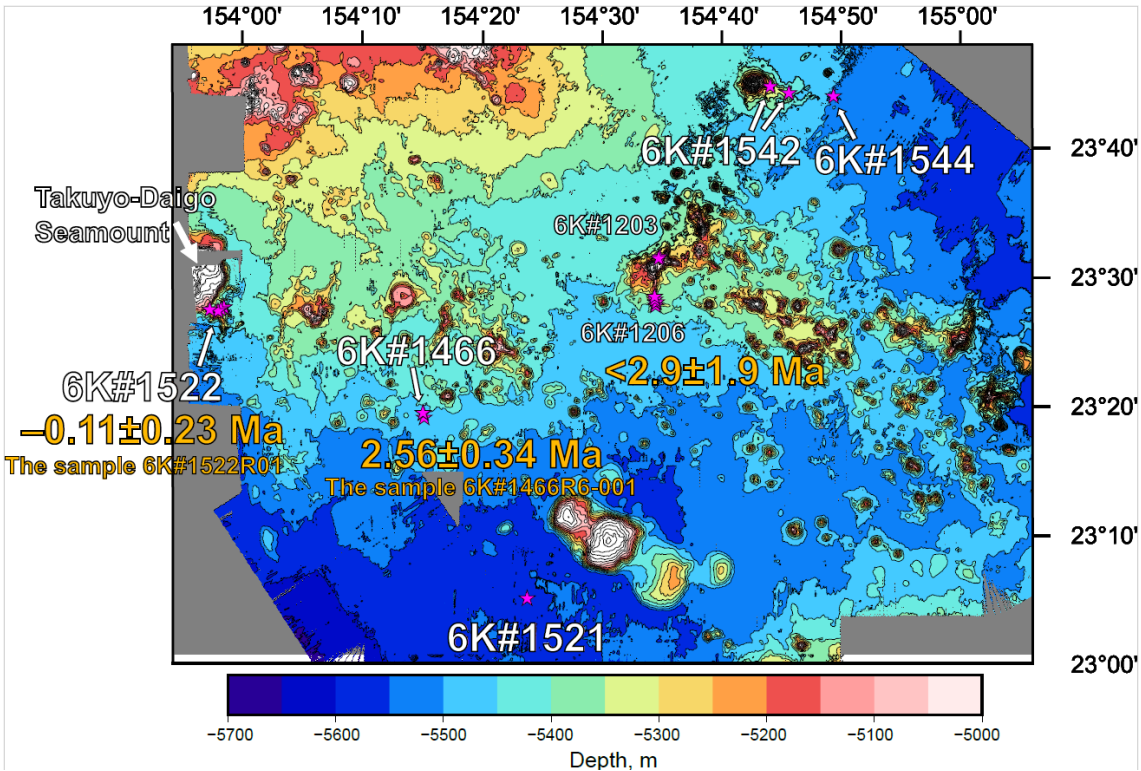
Fig. 2. Detailed bathymetry of the study area. The onboard multibeam data were surveyed during the YK10-05 and the YK18-08 cruises by the Japan Agency for Marine-Earth Science and Technology (JAMSTEC). The petit-spot knolls and outcrops were investigated during several dives as 6K#1466, 6K#1521, 6K#1522, 6K#1542, and 6K#1544. The pink-colored stars represent the sampling points. The age information was obtained in the present study and Hirano et al. (2019).

3 Field observations, sample locations, and petrography

186

Here, the eruptive sites of monogenetic volcanoes or lava outcrops are approximately along each dive site numbered 6K#1466, #1521, #1522, #1542, and #1544 conducted using the *Shinkai* 6500. Only the 6K#1466 dive was conducted at two types of monogenetic volcanoes, divided into the glassy (R3) and crystalline, vesicular (R6 and R7) types based on the geochemical and petrographic descriptions and occurrence of basaltic samples.

3.1 YK16-01 cruise and 6K#1466 dive

During the YK16-01 cruise, a small conical knoll (ca. 0.04 km^3) was investigated by a submersible dive, 6K#1466 (Figs. 2 and 3a). The lava flows, observed hollow lava tube resulting in sediment-rolling/disturbing eruption, were located approximately 600 m south of the top of the knoll (extremely fresh and glassy samples; 6K#1466R3-001 and R3-004 basalts) (Fig. 3a). Vesicular pillow basalts were collected on the western slope of the knoll (samples 6K#1466R6-001, R7-001, and R7-003; Fig. 3a). Although only the strong acoustic reflection could not completely distinguish the petit-spot lava fields in ferromanganese nodule fields, this dive revealed lava outcrops using a sub bottom profiler (SBP) and a multi narrow beam echo sounder (MBES). In detail, the petit-spot lava field, as an acoustically opaque layer, was identified by a vigorous backscattering intensity in the MBES with the distributions of the basement and sediment layers in the SBP.

The 6K#1466R3-001 and R3-004 samples were extremely fresh glassy basalts. The R3-001 and R3-004 basalts exhibited similar petrographic features (Fig. 3a). These basalts were covered by 3.0–4.5 mm-thick palagonite (hydrated quenched glass), and their outermost parts were surrounded by 5.8–7.2 mm-thick ferromanganese crust (Fig. 3a). They were less vesicular (<3 vol.%) and dominantly basaltic glass with euhedral–subhedral olivine microphenocrysts (~100–500 μm in size), ferrotitanium oxide (<50 μm in size), and minor plagioclase (~500 μm in size) (Fig. 3a). Secondary phases (e.g., clay minerals) were not observed.

The 6K#1466R6-001, R7-001, and R7-003 basalts, covered with 4.3–5.2 mm-thick ferromanganese crust over 5.5–6.6 mm-thick palagonite rinds, exhibited high vesicularity (20–40 vol.%) (Fig. 3a). Certain pyroxene-dominated xenocrysts and peridotite xenoliths have been reported by Mikuni et al. (2022). The basaltic groundmass comprised needle-shaped clinopyroxene (50–400 μm in size), subhedral olivine partly with aureoles of iddingsite (up to 100 μm in size), ferrotitanium oxide, minor spinel (up to 10 μm in size), glass, and crystallite, notably without remarkable phenocrysts (Fig. 3a). The photomicrograph of R6-001 is shown in Fig. 3a.

3.2 YK18-08 cruise and 6K#1521 and #1522 dives

Two submersible dives (6K#1521 and 1522) were conducted during the YK18-08 cruise to investigate petit-spot volcanoes. During the 6K#1521 dive, a small lava outcrop was discovered in the abyssal plain by tracing the strong acoustic reflection, which was expectedly derived from intrusive rock bodies, in the sedimentary layer detected by deep-sea SBP equipped on the *Shinkai* 6500. We observed that the strong reflective surface gradually became shallow during the navigation, revealing the small lava outcrop (Figs. 2 and 3b). Fresh and massive (nonvesicular) basalts were collected from this outcrop (samples 6K#1521R04 and R05; Fig. 3b). The samples from the 6K#1522 dive at a seamount exhibited highly irregular shapes, and massive lava flows, pillows, and lava breccia were observed (Fig. 3c). All the samples were fresh vesicular basalts (6K#1522R01, R02, R05, R12, R13, R16, and R17; Fig. 3c).

The fresh, massive, and nonvesicular basalts were obtained by 6K#1521 dive (R04 and R05) and comprised euhedral olivine microphenocrysts (150–400 μm in size), two types of ferrotitanium oxide (50–150 μm in size), and crystallite (Fig. 2b). Secondary phases were not observed as well. They were covered with 5.6–5.9 mm-thick ferromanganese crust and ~ 1.0 mm-thick palagonite rinds (Fig. 3b), but R05 did not have palagonite rinds. The photomicrograph of R04 is shown in Fig. 3b.

The seven fresh basalts collected during the 6K#1522 dive (6K#1522R01, R02, R05, R12, R13, R16, and R17), exhibited high vesicularity (20–40 vol.%) with 2.9–6.0 mm-thick palagonite rinds covered with 2.7–5.9 mm-thick ferromanganese crusts (Fig. 3c). Euhedral–subhedral olivine microphenocrysts (glomeroporphyritic, 30–200 μm in size), radial–needle-shaped clinopyroxene, iddingsite (<200 μm in size), spinel, and glass with minor xenocrystic olivines were observed (Fig. 3c). The photomicrograph of R01 is shown in Fig. 3c.

3.3 YK19-05S cruise and 6K#1542 and #1544 dives

A petit-spot knoll and related lava flows were surveyed by the 6K#1542 and #1544 dives, respectively, during the YK19-05S cruise (Fig. 2). During the 6K#1542 dive, geological survey and rock sampling were conducted from two points on the eastern slope of the knoll (Figs. 2 and 3d). Here, the 6K#1542R03 and R05 basalts were collected from the lava-breccia field covered with thin ferromanganese crust (Fig. 3d). Samples R06 and R09 were obtained from the lobate-surface lava between tubular lavas closer to the summit than R03 and R05 (Fig. 3d).

High-resolution (one-meter scale) bathymetric mapping was successfully conducted during the 6K#1544 dive, and this can contribute to future oceanographic investigations using the Human Occupied Vehicle (Kaneko et al., 2022). During this acoustic survey, several mounds, 10–20 m in height and a few hundred meters in diameter, were recognized (Fig. 3d). We observed these mounds and collected samples from outcrops during the second half of the dive. Pillow lavas, tumuli, and lava breccias were observed, and basaltic samples (6K#1544R04, R05, and R06) were collected (Fig. 3d).

258   Four vesicular basalts (10–30 vol.% vesicularity; 6K#1542R03, R05, R06, and R09) were

259   covered with 4.3–4.4 mm-thick ferromanganese crust. The outer palagonitic rinds were 3.2–3.4 mm-

260   thick (Fig. 3d). A few to 300-μm-sized euhedral–subhedral olivine microlites and microphenocrysts

261   were glomeroporphyritic (Fig. 3d). The groundmass was dominated by needled dendritic

262   clinopyroxenes (~100 μm in size). The others were olivine, spinel, glass, and xenocrystic olivine

263   megacrysts. The photomicrograph of R06 is shown in Fig. 3d.

264   The basaltic samples from the 6K#1544 dive (6K#1544R04, R05, and R06) were covered with

265   ferromanganese crust (5.0–5.8 mm-thick) over palagonitic rinds (3.4–4.4 mm-thick). All the samples

266   exhibited high vesicularity in the range of 20–35 vol.% (Fig. 3d). They comprised olivine

267   microphenocrysts (30–250 μm in size, euhedral–subhedral or columnar), clinopyroxene (<100 μm,

268   needled, columnar, radial or dendritic shape), spinel, and glass without secondary phases (Fig. 3d).

269   The photomicrograph of R04 is shown in Fig. 3d. During macroscopic observations, practically

270   all the basalts from the 6K#1542 and 6K#1544 dives exhibited similar vesicularity and freshness.

271   Their geochemical features were also similar to each other and are described in Sect. 5-1 and 5-2.

272

273

(b)

274

(c)

275
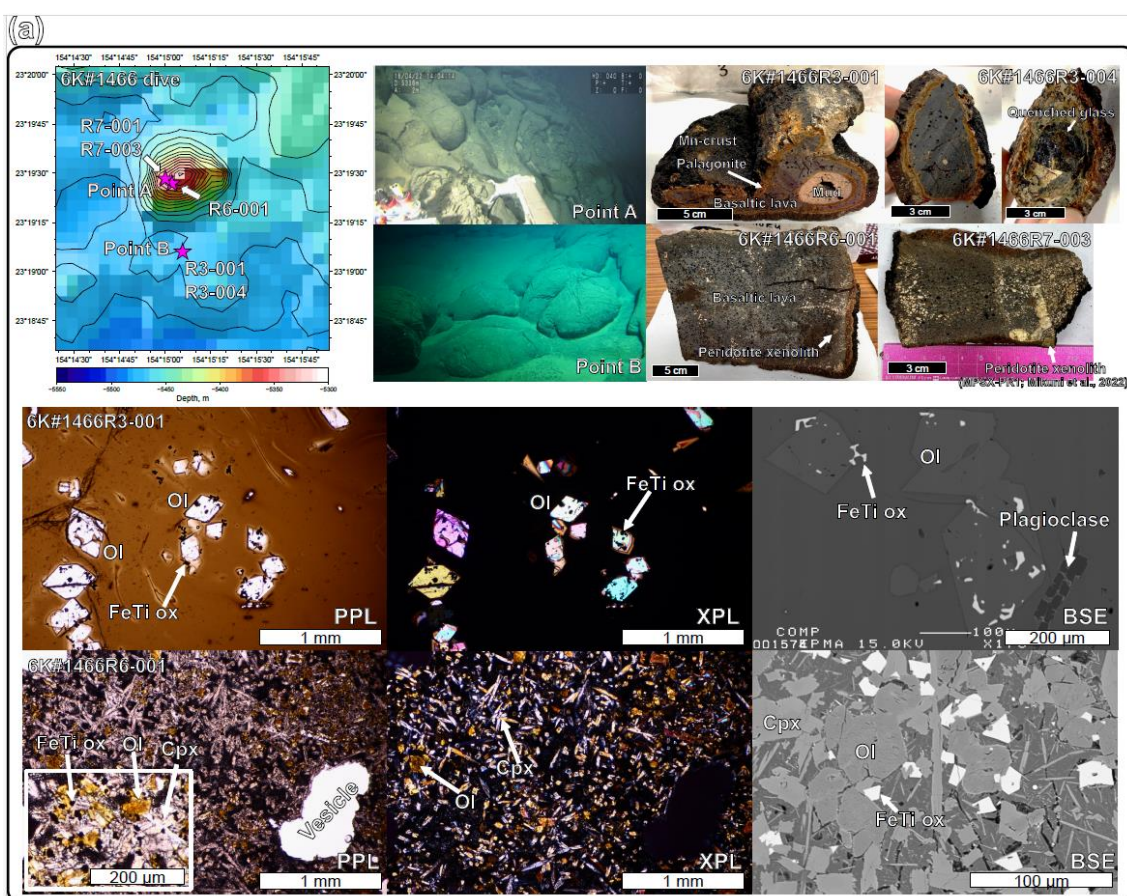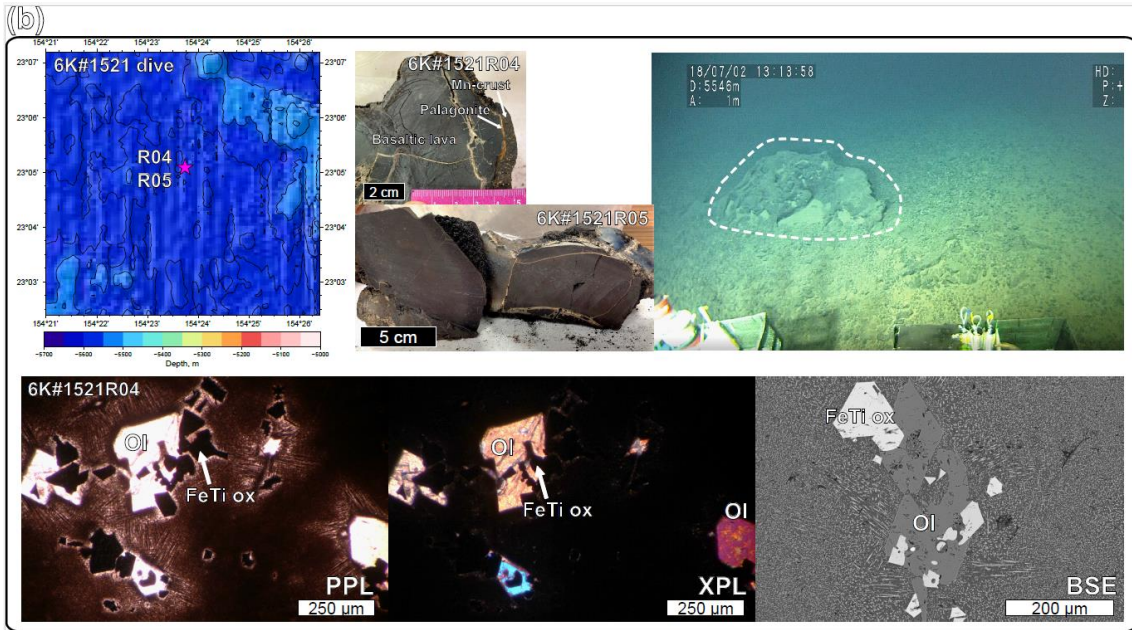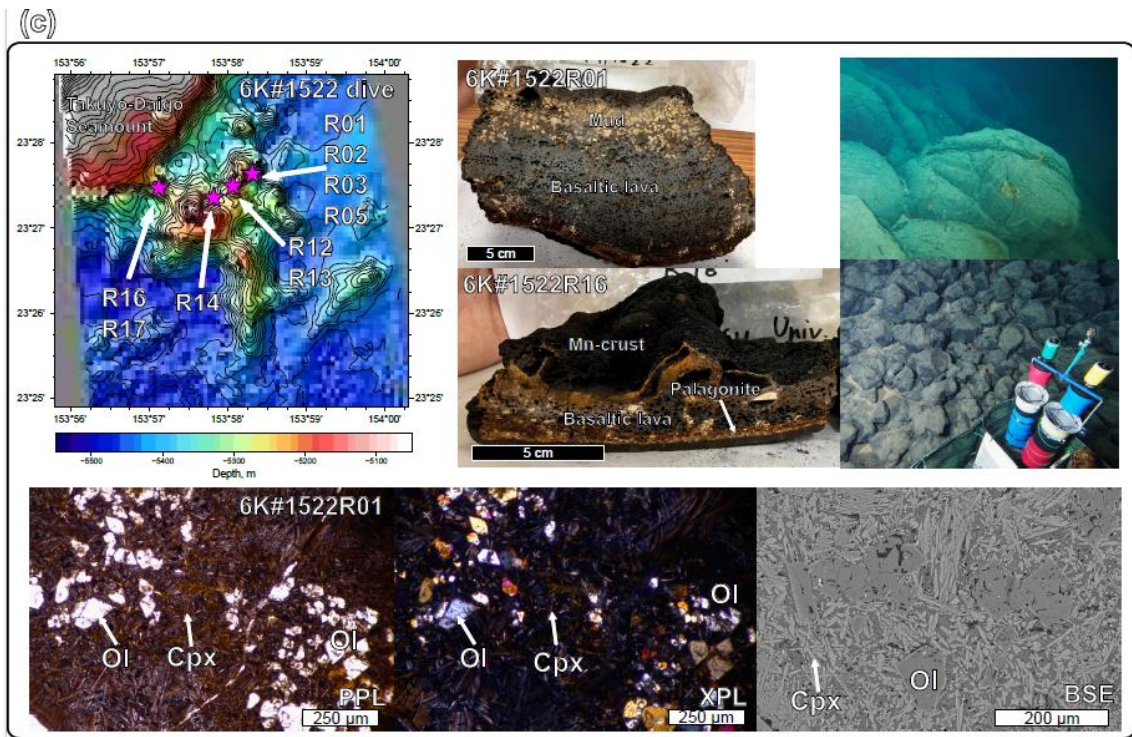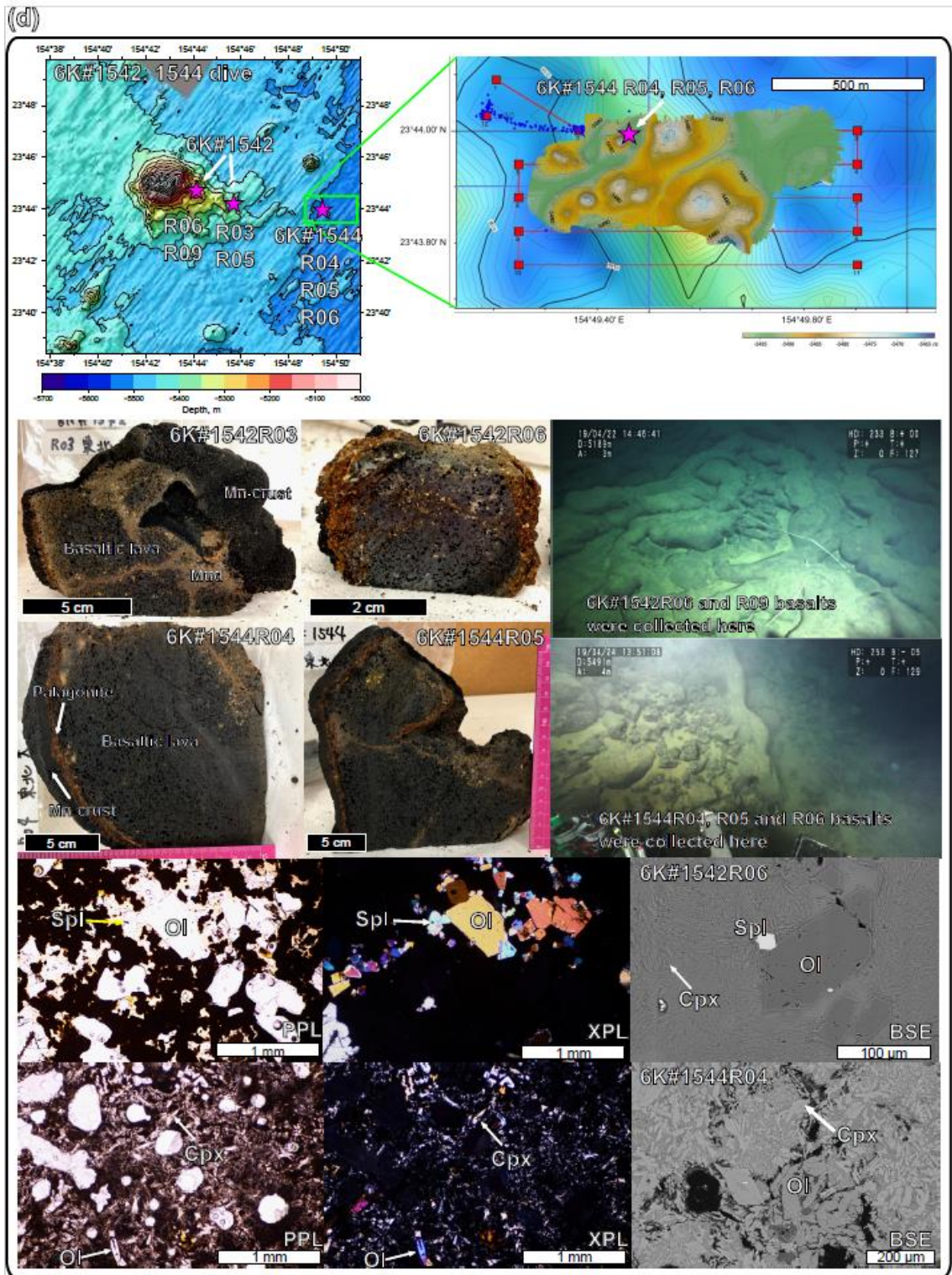
Fig. 3. Bathymetric map with photos of the outcrop, the collected samples, and their photomicrographs with detailed bathymetry of the sampling points. (a) The 6K#1466, (b) 6K#1521, (c) 6K#1522, and (d) 6K#1542 and 6K#1544 dives using the *Shinkai* 6500 by JAMSTEC. The 1-m gridded bathymetry of the 6K#1544 dive is shown in (d), obtained using an MBES equipped with the *Shinkai* 6500 over a 100-m resolution map

281 obtained using the surface ship, R/V *Yokosuka* (Kaneko et al., 2022). The photomicrographs of

282 representative samples are shown for plane-polarized light (PPL), cross-polarized light (XPL), and

283 backscatter electron (BSE). Ol, olivine; Cpx, clinopyroxene; Mgt, magnetite; Spl, spinel.

284

285

286 **4. Analytical methods**

287

288 **4.1 Major and trace element analysis of volcanic glass, mineral, and whole-rock**

289

290 Major element compositions of glasses and minerals were determined using an electron probe

291 micro analyzer (EPMA). JXA-8900R at Atmosphere and Ocean Research Institute (AORI), the

292 University of Tokyo was used for glass analysis and JXA-iHP200F at GSJ, AIST was used for mineral

293 analysis. The analyses were performed using an accelerating voltage of 15 kV, a beam current of 12

294 nA, and a beam diameter of 10 μm for glass and 2 μm for mineral. A peak counting time of 20 s and

295 a background counting time of 10 s were used, except for Ni, for which a peak counting time of 30 s

296 and a background counting time of 15 s. For Na analysis of glass, the peak counting time was 5 s and

297 the background counting time was 2 s. Natural and synthetic minerals were used as standards, and data

298 were corrected using a ZAF online correction program (Akizawa et al., 2021). Major element

299 composition of glass was determined by the mean value of 10 analytical points.

300 Trace element compositions of minerals were determined using a laser ablation-inductively

301 coupled plasma-mass spectrometry (LA-ICP-MS; New Wave Research UP-213 and Agilent 7500s)

302 at Kanazawa University. The Nd: YAG deep UV (ultraviolet) laser's wavelength is 213 nm. The

303 analyses were conducted with 100 μm spot size. A repetition frequency of 6 Hz and a laser energy

304 density of 8 J cm^{-2} were used. NIST612 glass (distributed by National Institute of Standards and

305 Technology) was employed for calibration, using the preferred values of Pearce et al. (1997). Data

306 reduction was undertaken with ^{29}Si as the initial standard, and SiO_2 concentrations were obtained by

307 an electron microprobe analysis (Longerich et al., 1996). BCR-2G (distributed by the United States

308 Geological Survey) was used as a secondary standard to assess the precision of each analytical

309 session (Jochum and Nohl, 2008).

310 Whole-rock major and trace element compositions of rock samples were analyzed by Activation

311 Laboratories Ltd., Canada, using Code 4Lithoresearch Lithogeochemistry and ultratrace5 Exploration

312 Geochemistry Package. The former package uses lithium metaborate/tetraborate fusion with

313 inductively coupled plasma optical emission spectrometry (FUS-ICP-OES) and inductively coupled

314 plasma mass spectroscopy (FUS-ICP-MS) for the major and trace element analyses, respectively. The

315 latter package uses inductively coupled plasma optical emission spectrometry (ICP-OES) and

316 inductively coupled plasma mass spectroscopy (ICP-MS) for the major and trace element analyses,

317 respectively.

318

319 **4.2 Sr, Nd, and Pb isotope analysis**

320

321 **4.2.1 Acid leaching**

322

323   Acid leaching was conducted for the selected basaltic samples on the basis of the procedure of
324 Weis and Frey (1991, 1996) as follows: [1] About 0.3–0.4 or 0.6 g of rock powder is weighed into an
325 acid-washed 15 mL Teflon vial (Savilex®). [2] 10 or 12 mL of 6N (N: normality) HCl were added, and
326 then heated at 80°C for 20–30 min. [3] After heating, the suspension is ultra-sonicated in 60°C water
327 for 20 min. [4] The supernatant is decanted. Steps [2] to [4] were repeated more than 4 times (up to 6
328 times) until the supernatant become clear or pale yellow to colorless. [5] TAMAPURE-AA Ultrapure
329 water (Tama Chemicals; Co., Ltd.), which includes a lower Pb blank than milli-Q H_2O, were added
330 instead of 6N HCl, and the suspension is ultra-sonicated for 20 min. This step is conducted twice. [6]
331 The leached rock powder is dried on a hot plate at 120°C. [7] After cooling, the powder is weighed.

332

333 **4.2.2 Extraction of Pb, Sr, and Nd**

334

335   The extraction of Pb, Sr, and Nd was performed following the procedures of Tanimizu and
336 Ishikawa (2006) and Machida et al. (2009). First, from ~50 to ~100 mg of rock powder was weighted
337 in a 7 mL Teflon vial (designated as "vial A"), and digested using mixed acid composed of HF and
338 HBr. The separation was conducted by cation exchange resin (AG-1X8; Bio-Rad Laboratories Inc.)
339 on the basis of procedures described in Tanimizu and ishikawa (2006). All fractions from the first and
340 second supernatant loading (0.5 M HBr) to the elution of other elements (mixed acid composed of
341 0.25 M HBr and 0.5 M HNO_3) were collected in another 7 mL Teflon vial (designated as "vial B") for
342 Sr and Nd separation. Finally, Pb was extracted by 1 mL of 1M HNO_3 in another 7 mL Teflon vial
343 (designated as "vial C"). The procedural blanks for Pb totaled less than 23 pg.
344   The Sr and Nd-bearing solution in the vial B was transferred into the vial A containing residues
345 of digested samples. 2 mL of $HClO_4$ and 2 mL HNO_3 was further added to the vial A, and the residue
346 was dissolved at 110 °C. Both Sr and Nd were separated by column with a cation exchange resin
347 (AG50W-8X; Bio-Rad Laboratories Inc.) and a Ln resin (Eichrom Tech- nologies Inc.) on the basis of
348 procedures described in Machida et al. (2009). The separated Sr and Nd were further purified by
349 column separation with a cation exchange resin. The total procedural blanks for Sr and Nd were less
350 than 100 pg.

351

352 **4.2.3 Analytical procedure**

353

Pb isotopic ratios were obtained using the multi-collector ICP-MS (MC-ICP-MS; Neptune plus, Thermo Fisher Scientific), with nine Faraday collectors, at Chiba Institute of Technology (CIT), Japan. The NIST SRM-981 Pb standard was also analyzed and yielded the average values of $^{206}Pb/^{204}Pb$ = 16.9303 ± 0.0005, $^{207}Pb/^{204}Pb$ = 15.4828 ± 0.0006, and $^{208}Pb/^{204}Pb$ = 36.6710 ± 0.0016. These correspond to previous values determined using MC-ICP-MS with Tl normalization, but they were slightly lower than values determined by TIMS in Tanimizu and Ishikawa (2006) from the $^{207}Pb-^{204}Pb$ double-spike. Reproducibility was monitored by an analyses of the JB-2 GSJ standard, and the obtained values were $^{206}Pb/^{204}Pb$ = 18.3326 ± 0.0005, $^{207}Pb/^{204}Pb$ = 15.5453 ± 0.0006, and $^{208}Pb/^{204}Pb$ = 38.2240 ± 0.0017.

Sr and Nd isotopic analyses for powdered rocks and glasses were conducted using the thermal ionization mass spectrometry (TIMS; Triton XT, Thermo Fisher Scientific) with nine Faraday collectors, at CIT. 1.5 µL of 2.5M HCl and 0.5M HNO_3 was used for loading of separated Sr and Nd of sample on the single and double Re-filament, respectively. The measured isotopic ratios were corrected for instrumental fractionation by adopting the $^{86}Sr/^{85}Sr$ value to be 0.1194 and that of $^{146}Nd/^{144}Nd$ to be 0.7219. The average value for the NIST SRM-987 Sr standard was 0.710239 ±0.000005 (2σ, n =2), and that for the GSJ JNdi-1 Nd standard was 0.512103 ±0.000005 (2σ, n =2). They agree well with values from the literature for the NIST SRM-987 ($^{87}Sr/^{86}Sr$ = 0.710252–0.710256; Weis et al., 2006) and JNdi-1 ($^{143}Nd/^{144}Nd$ = 0.512101; Wakaki et al., 2007). Consequently, we did not correct the values of the unknowns for offsets between the measurements and the values for the Sr and Nd standards.

374

4.3 $^{40}Ar/^{39}Ar$ dating

376

Samples for $^{40}Ar/^{39}Ar$ dating were prepared by separating crystalline groundmass after crushing them to sizes between 100 and 500 µm. The separated groundmass samples were leached by HNO_3 (1 mol/L) for one hour to remove clays and altered materials. All samples were wrapped in aluminum foil along with JG-1 biotite (Iwata, 1998), K_2SO_4, and CaF_2 flux monitors. Any amorphous (e.g., quenched glass) was removed because ^{39}Ar may move from one phase to another in a process known as "recoil." This can create a disturbed age spectrum when ^{39}Ar is produced from ^{39}K in amorphous material through interaction with fast neutrons during irradiation of the sample. Samples were irradiated for 6.6 days in the Kyoto University Research Reactor (KUR), Kyoto University. Argon extraction and isotopic analyses were undertaken at the Graduate School of Arts and Sciences, the University of Tokyo. The sample gases were extracted by incremental heating of 10 or 11 steps between 600°C and 1500°C. The analytical methods used are the same as those used by Ebisawa et al. (2004) and Kobayashi et al. (2021).

5 Results

391

To describe the geochemical and chronological results, each sample group was denoted by its dive number, e.g., the sample group obtained from the 6K#1521 dive was labeled "1521 samples". The basalts from the 6K#1466 dive were divided into two groups for R3 (collected from the seafloor south of the knoll) and R6–R7 (sampled on the knoll) based on their geographical, petrological, and compositional differences. The mineral compositions of each petit-spot basalt are shown in Fig. S1 and Table S1, S2 and S3.

398

5.1 Major and trace element compositions

400

The major and trace element compositions for the whole rock and glass of the petit-spot basalts are listed in Table 2 and 3, respectively. The basalt compositions for a petit-spot knoll were reported by Hirano et al. (2019) (expressed as "1203, 1206" in each figure). The data are discussed along with the reported NW Pacific petit-spots (Hirano and Machida, 2022). Using a total alkali vs. silica (TAS) diagram, virtually all the samples were classified as alkalic rocks, but the 1542 and 1544 basalts were plotted near the boundary between alkalic and non-alkalic (Fig. 4a). Two petit-spot basalts (1466R7-001 and R7-003) from the petit-spot knoll were notably silica-undersaturated (i.e., SiO_2 = 39.3–39.4 wt%) and classified as foidite (Mikuni et al., 2022). All the western Pacific petit-spot basalts, except for the 6K#1466R7 basalts, were sodic (K_2O/Na_2O = 0.24–0.58) and were notably discriminated to the potassic NW Pacific petit-spots (Fig. 4b).

Selected major element oxides and trace element ratios vs. MgO plots for the petit-spot basalts are shown in Figs. 5 and 6, respectively. The MgO concentrations of the 1466R3 and 1521 samples each exhibiting similar petrographic features (i.e., nonvesicular, and glassy) were characterized by values (4.0–4.4 wt%) lower than those of other vesicular samples (6.6–9.3 wt%). The K_2O, Na_2O, Al_2O_3, and SiO_2 contents negatively correlated with MgO (Figs. 5a–d). The CaO, FeO_T, and CaO/Al_2O_3 abundances exhibited positive correlations with MgO (Figs. 5e–g). The TiO_2 concentrations exhibited no correlations with MgO (Fig. 5h), as well as the selected trace element ratios (Figs. 6a–g) except for the Sm/Hf ratio with positive correlations (Fig. 6h). The Sm/Hf ratio also negatively correlated with SiO_2 (Fig. S2). The study samples exhibited whole-rock loss on ignition (LOI) in the range of 0.67–1.72 wt%, excluding two relatively altered samples, 6K#1466R7-001 (LOI = 2.68 wt%) and R7-003 (LOI = 6.29 wt%).

The PM-normalized (Sun and McDonough, 1989) trace element patterns for the petit-spot basalts, including those reported by a previous study (Hirano et al., 2019), were shown for each dive compared to the representative ocean island basalt (OIB) in Figs. 7a–f. The petit-spot basalts generally

showed high light rare earth element (LREE)/heavy REE (HREE) ratios. Negative Zr, Hf, Ti, and Y

anomalies were commonly observed in these western Pacific petit-spots as well as those of the NW

Pacific petit-spots (Fig. 7g). The 1466 basalts collected on the seafloor south of the knoll (6K#1466R3-

001 and R3-004) were compositionally different from those obtained on the knoll (6K#1466R7-001,

R7-003). The basalts from the 6K#1542 and 1544 dives, collected from nearby locations, had the same

compositions in major and trace element ratios in both whole rock and glass, respectively (Figs. 4, 5,

6, 7e, and f). These samples in the Ba/Nb and Sm/Hf diagrams were plotted in the range of "Group 3"

in the discrimination of the NW Pacific petit-spot basalts (Machida et al., 2015), indicating their

negative Zr and Hf anomalies without notable U, Th, Nb, and Ta anomalies in the PM-normalized

trace element patterns (Fig. 7h). The Sm/Hf ratio of the differentiated 1466R3 samples was lower than

that of other samples. A positive correlation between fluid mobile and immobile elements, Ba vs. Nb

(Fig. 8a) and U vs. Th (Fig. 8b), respectively, was observed, excluding the Ba of the 1466R7 samples

(Fig. 8a).

Table. 2
Major and trace element compositions of western Pacific petit-spot basalts.

Cruise	YK16-01		YK16-01		YK16-01	YK16-01	YK18-08		YK18-08		YK18-08		YK18-08	YK18-08		YK18-08		YK18-08	
Sample name	6K#1466R3-001		6K#1466R3-004		6K#1466R7-001	6K#1466R7-003	6K#1521R04		6K#1521R05		6K#1522R01		6K#1522R01	6K#1522R02		6K#1522R05		6K#1522R12	
Sample type	Glass		Glass		Whole rock	Whole rock	Glass		Glass		Glass		Whole rock	Glass		Glass		Glass	
Method	EPMA		EPMA		*	*	EPMA		EPMA		EPMA		*	EPMA		EPMA		EPMA	
	mean of n=10	2σ	mean of n=10	2σ			mean of n=10	2σ	mean of n=10	2σ	mean of n=10	2σ		mean of n=10	2σ	mean of n=10	2σ	mean of n=10	2σ
wt%																			
SiO$_2$	51.56	0.93	50.63	0.79	39.40	39.27	48.42	0.36	46.78	0.97	45.92	1.40	45.28	45.90	0.79	45.38	1.56	46.02	0.69
TiO$_2$	2.31	0.20	2.19	0.22	3.82	3.68	3.65	0.30	3.32	0.25	2.37	0.17	2.43	2.51	0.20	2.33	0.13	2.45	0.21
Al$_2$O$_3$	14.99	0.57	15.10	0.37	11.41	11.46	15.12	0.31	14.38	0.45	12.74	0.23	12.48	12.82	0.25	11.99	0.53	12.91	0.14
Cr$_2$O$_3$	-	-	-	-	0.03	0.03	-	-	-	-	0.01	0.05	0.03	0.02	0.05	0.01	0.05	0.02	0.04
FeO^T	9.68	0.30	9.17	0.62	15.12	14.90	10.65	0.29	9.77	0.79	11.72	0.16	12.32	11.64	0.42	10.77	1.02	11.62	0.20
MnO	0.14	0.04	0.14	0.05	0.21	0.20	0.16	0.04	0.14	0.03	0.18	0.04	0.18	0.16	0.04	0.15	0.05	0.17	0.05
MgO	4.04	0.11	3.99	0.11	9.34	7.66	4.43	0.08	4.36	0.10	7.36	0.17	7.26	7.33	0.10	7.12	0.23	7.14	0.16
CaO	7.71	0.11	7.41	0.25	11.19	10.02	8.34	0.68	7.80	0.29	10.72	0.14	11.18	10.81	0.22	10.33	0.68	10.79	0.10
Na$_2$O	4.61	0.24	4.38	0.50	2.15	2.29	3.84	0.31	4.05	0.55	4.16	0.21	3.53	4.16	0.29	4.16	0.24	4.01	0.46
K$_2$O	2.31	0.08	2.24	0.12	1.65	2.08	2.25	0.27	2.13	0.12	1.38	0.06	1.42	1.40	0.13	1.31	0.10	1.38	0.04
NiO	0.01	0.03	0.01	0.03	0.03	0.02	-	0.04	-	0.05	0.02	0.03	0.02	0.01	0.04	0.02	0.04	0.02	0.04
P$_2$O$_5$	0.93	0.03	0.91	0.06	1.08	1.12	1.53	0.11	1.51	0.03	0.80	0.06	0.83	0.80	0.08	0.82	0.06	0.77	0.04
Total	98.28		96.16		98.10	99.02	98.38		94.24		97.35		98.67	97.56		94.40		97.31	
Mg#	42.64		43.68		52.42	47.82	42.57		44.33		52.83		51.24	52.89		54.11		52.28	
LOI					2.68	6.29							1.72						

FeO^T as total values.
Mg# = 100 x Mg / [Mg+Fe^{2+}]$_{molar}$.
" - ": not detected
*: Analyzed by ActLab

Table. 2 continued

	YK18-08		YK18-08		YK18-08		YK19-05S		YK19-05S	YK19-05S		YK19-05S		YK19-05S		YK19-05S		YK19-05S	YK19-05S		YK19-05S	
	6K#1522R13		6K#1522R16		6K#1522R17		6K#1542R03		6K#1542R03	6K#1542R05		6K#1542R06		6K#1542R09		6K#1544R04		6K#1544R04	6K#1544R05		6K#1544R06	
	Glass		Glass		Glass		Glass		Whole rock	Glass		Glass		Glass		Glass		Whole rock	Glass		Glass	
	EPMA		EPMA		EPMA		EPMA		*	EPMA		EPMA		EPMA		EPMA		*	EPMA		EPMA	
	mean of n=10	2σ	mean of n=10	2σ	mean of n=10	2σ	mean of n=10	2σ		mean of n=10	2σ	mean of n=10	2σ	mean of n=10	2σ	mean of n=10	2σ		mean of n=10	2σ	mean of n=10	2σ
SiO$_2$	47.09	0.68	45.22	0.73	45.06	0.98	48.66	1.14	49.35	48.77	1.51	49.66	1.11	50.09	0.93	50.54	0.43	49.08	50.53	0.61	49.59	1.18
TiO$_2$	2.50	0.20	2.58	0.20	2.67	0.27	2.11	0.19	2.16	2.13	0.18	2.25	0.22	2.24	0.20	2.04	0.23	2.13	2.08	0.25	2.07	0.24
Al$_2$O$_3$	13.08	0.33	12.55	0.17	12.55	0.14	13.49	0.18	12.52	13.38	0.19	12.55	0.43	12.78	0.33	13.18	0.12	13.25	12.94	0.34	12.94	0.36
Cr$_2$O$_3$	0.02	0.05	0.01	0.04	0.02	0.08	0.04	0.05	0.05	0.03	0.07	0.02	0.04	0.04	0.04	0.03	0.05	0.05	0.03	0.05	0.03	0.04
FeO^T	11.74	0.49	11.94	0.40	11.89	0.26	10.60	0.30	11.40	10.47	0.36	10.22	0.51	10.44	0.34	10.46	0.34	11.13	10.77	0.37	10.53	0.49
MnO	0.17	0.05	0.18	0.05	0.18	0.05	0.15	0.04	0.17	0.14	0.04	0.15	0.04	0.16	0.04	0.16	0.02	0.16	0.16	0.05	0.15	0.05
MgO	6.63	0.64	7.24	0.25	7.24	0.17	7.29	0.17	8.18	7.29	0.20	7.03	0.13	7.11	0.12	7.00	0.16	7.50	7.10	0.15	7.05	0.15
CaO	11.01	0.25	11.17	0.24	11.19	0.25	10.03	0.14	10.74	10.00	0.10	9.90	0.32	10.03	0.24	10.63	0.26	10.67	10.36	0.17	10.33	0.22
Na$_2$O	4.16	0.36	4.30	0.33	4.28	0.39	3.30	0.28	2.59	3.36	0.24	3.39	0.19	3.26	0.46	3.54	0.25	2.90	3.52	0.26	3.42	0.28
K$_2$O	1.42	0.17	1.52	0.08	1.51	0.06	0.80	0.05	0.77	0.80	0.06	0.89	0.04	0.91	0.06	0.85	0.08	0.85	0.85	0.06	0.83	0.04
NiO	0.01	0.04	0.01	0.04	0.01	0.04	0.01	0.05	0.02	0.02	0.05	0.02	0.05	0.03	0.05	0.02	0.03	0.02	0.01	0.04	0.02	0.04
P$_2$O$_5$	0.83	0.05	0.95	0.07	0.95	0.03	0.48	0.04	0.50	0.50	0.04	0.51	0.04	0.52	0.06	0.54	0.03	0.52	0.57	0.05	0.55	0.04
Total	98.66		97.67		97.54		96.96		99.12	96.91		96.62		97.60		98.98		99.09	98.91		97.50	
Mg#	50.18		51.93		52.04		55.07		56.13	55.38		55.07		54.83		54.39		54.57	54.04		54.41	
LOI									0.67									0.83				

Table 3

µg/g	YK16-01 6K#1466R3-001 Glass LA-ICPMS	YK16-01 6K#1466R3-004 Glass LA-ICPMS	YK16-01 6K#1466R7-001 Whole rock *	YK16-01 6K#1466R7-003 Whole rock *	YK18-08 6K#1521R04 Glass LA-ICPMS	YK18-08 6K#1521R05 Glass LA-ICPMS	YK18-08 6K#1522R01 Glass LA-ICPMS	YK18-08 6K#1522R01 Whole rock *	YK18-08 6K#1522R02 Glass LA-ICPMS	YK18-08 6K#1522R05 Glass LA-ICPMS	YK18-08 6K#1522R12 Glass LA-ICPMS
Li	7.60	7.32			7.39	7.00	8.10		7.69	7.83	7.71
B	2.92	3.17			3.05	3.48	2.38		2.34	2.78	2.69
Sc	14.9	15.2	25.0	25.0	15.7	15.4	20.1	21.0	20.6	21.2	21.1
V	159	160	353	324	167	157	204	234	208	207	207
Cr	36.8	37.1	200	190	0.52	0.48	215	190	218	213	222
Co	29.7	29.9	61.0	57.0	32.8	31.2	46.2	49.0	46.8	46.1	47.3
Rb	47.5	47.6	26.0	32.0	34.1	33.4	25.8	28.0	26.9	26.8	26.6
Sr	976	991	577	307	1385	1361	848	827	924	943	901
Y	21.8	22.2	37.0	58.0	33.1	32.2	24.4	25.0	26.0	27.6	26.7
Zr	254	260	259	248	293	286	157	163	168	177	171
Nb	56.4	57.5	65.0	64.0	58.7	57.6	49.5	52.0	55.3	55.7	54.6
Cs	0.58	0.58	-	-	0.35	0.34	0.32	-	0.35	0.37	0.34
Ba	613	623	453	317	577	565	447	479	512	528	500
La	44.1	45.4	65.2	90.8	44.2	42.8	42.8	51.5	49.6	51.4	48.6
Ce	93.2	95.0	138	164	105	101	88.1	110	101	103	98.3
Pr	10.6	10.8	16.6	23.8	13.4	13.0	9.9	12.4	11.3	11.6	11.2
Nd	42.5	43.7	62.6	89.3	59.5	57.6	39.4	47.4	45.5	47.5	45.7
Sm	8.39	8.65	12.0	17.6	12.8	12.3	8.27	10.1	9.60	9.83	9.60
Eu	2.78	2.83	3.76	5.38	4.17	4.03	2.72	3.39	3.13	3.19	3.14
Gd	7.08	7.23	10.7	15.7	11.0	10.6	7.12	9.20	8.27	8.93	8.53
Tb	0.89	0.94	1.50	2.30	1.40	1.35	0.93	1.30	1.08	1.14	1.10
Dy	4.84	4.99	8.00	12.2	7.55	7.31	5.05	6.60	5.94	6.23	6.05
Ho	0.79	0.81	1.30	2.10	1.24	1.19	0.82	1.10	0.97	1.01	1.00
Er	1.96	2.04	3.30	5.30	3.01	2.94	2.03	2.60	2.37	2.53	2.41
Tm	0.23	0.25	0.44	0.69	0.34	0.34	0.22	0.31	0.26	0.29	0.27
Yb	1.43	1.48	2.60	4.10	2.12	2.02	1.40	1.70	1.64	1.71	1.69
Lu	0.19	0.19	0.36	0.60	0.28	0.26	0.18	0.24	0.22	0.23	0.22
Hf	5.33	5.54	5.80	6.20	6.42	6.12	3.14	3.90	3.76	4.01	3.92
Ta	3.04	2.81	4.80	5.30	3.34	2.93	2.01	2.80	2.34	2.35	2.37
Pb	3.55	3.39	-	6.00	2.82	2.59	3.06	-	3.68	3.64	3.59
Th	4.87	5.11	6.90	7.70	3.52	3.40	4.65	6.40	5.73	6.07	5.69
U	1.29	1.29	1.40	7.70	0.97	0.91	1.08	6.40	1.28	1.27	1.26

* - *: not detected
*: Analyzed by ActLab

Table. 3 continued

	YK18-08 6K#1522R13 Glass LA-ICPMS	YK18-08 6K#1522R16 Glass LA-ICPMS	YK18-08 6K#1522R17 Glass LA-ICPMS	YK19-05S 6K#1542R03 Glass LA-ICPMS	YK19-05S 6K#1542R03 Whole rock *	YK19-05S 6K#1542R05 Glass LA-ICPMS	YK19-05S 6K#1542R06 Glass LA-ICPMS	YK19-05S 6K#1542R09 Glass LA-ICPMS	YK19-05S 6K#1544R04 Glass LA-ICPMS	YK19-05S 6K#1544R04 Whole rock *	YK19-05S 6K#1544R05 Glass LA-ICPMS	YK19-05S 6K#1544R06 Glass LA-ICPMS
Li	8.06	8.53	8.42	5.54		5.52	6.00	6.19	6.21		6.20	6.16
B	2.83	2.77	2.94	1.60		1.88	1.89	1.80	2.28		2.38	2.14
Sc	21.5	19.7	20.6	22.5	24.0	22.3	22.7	23.7	22.0	22.0	22.8	23.6
V	217	213	209	189	222	188	200	201	203	215	197	191
Cr	231	203	203	334	350	317	269	267	292	330	285	273
Co	44.3	47.2	46.8	42.3	49.0	42.7	42.1	41.8	44.9	47.0	43.4	42.0
Rb	28.0	30.3	29.7	14.2	14.2	14.5	17.4	17.4	17.0	17.0	16.4	16.4
Sr	930	1063	1086	565	487	568	622	643	579	519	595	604
Y	27.0	27.9	29.6	22.8	20.0	22.4	22.5	23.7	22.9	21.0	24.0	25.1
Zr	173	184	194	122	120	122	134	140	123	122	128	132
Nb	55.7	64.2	65.7	24.0	23.0	24.0	25.1	25.9	27.0	25.0	27.3	27.4
Cs	0.36	0.41	0.40	0.18		0.20	0.22	0.21	0.25		0.25	0.23
Ba	514	584	590	255	219	254	292	301	286	259	297	297
La	49.3	58.1	60.9	26.8	26.1	26.6	28.6	29.8	27.8	28.0	28.8	29.5
Ce	101	120	122	56.6	62.8	56.5	58.8	60.4	59.8	66	60.9	60.0
Pr	11.5	13.3	13.8	6.86	7.37	6.79	7.10	7.42	7.20	7.60	7.34	7.41
Nd	46.6	53.3	55.7	29.3	30.0	29.0	30.3	31.7	30.4	31.3	31.3	31.8
Sm	9.71	10.8	11.4	6.65	7.00	6.64	6.82	7.21	6.79	7.10	7.10	7.27
Eu	3.21	3.58	3.67	2.24	2.41	2.23	2.28	2.38	2.34	2.42	2.39	2.44
Gd	8.57	9.42	9.92	6.29	6.80	6.26	6.53	6.82	6.45	6.90	6.75	6.90
Tb	1.12	1.20	1.27	0.85	1.00	0.85	0.87	0.93	0.89	1.00	0.91	0.96
Dy	6.10	6.38	6.81	4.89	5.30	4.83	4.88	5.10	4.91	5.40	5.17	5.33
Ho	1.00	1.02	1.10	0.83	0.90	0.82	0.84	0.87	0.84	0.90	0.89	0.91
Er	2.46	2.47	2.63	2.12	2.30	2.13	2.10	2.22	2.10	2.30	2.27	2.32
Tm	0.28	0.28	0.30	0.26	0.28	0.26	0.26	0.26	0.26	0.29	0.28	0.27
Yb	1.70	1.67	1.75	1.57	1.70	1.57	1.52	1.60	1.58	1.70	1.66	1.71
Lu	0.22	0.21	0.22	0.21	0.23	0.21	0.20	0.22	0.21	0.22	0.23	0.23
Hf	3.95	4.08	4.36	2.95	3.10	2.95	3.20	3.39	2.95	3.00	3.12	3.18
Ta	2.40	2.63	2.77	1.08	1.30	1.10	1.16	1.23	1.21	1.40	1.23	1.24
Pb	3.71	4.38	4.29	1.67		1.76	1.82	1.85	1.94		1.98	1.82
Th	5.69	6.88	7.29	2.47	2.80	2.47	2.78	2.89	2.72	3.00	2.85	2.95
U	1.31	1.57	1.58	0.62	2.80	0.63	0.66	0.66	0.71	3.00	0.68	0.65
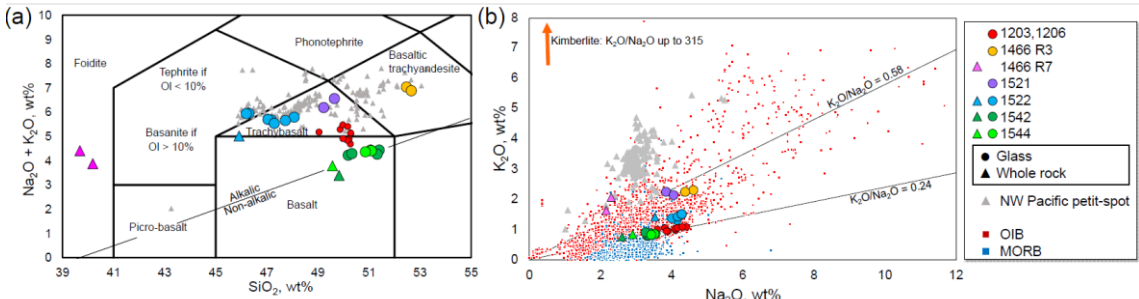
Fig. 4. Relationships between the SiO₂ and alkali contents. (a) Total alkali vs. silica diagram using the platform of Le Bas et al. (1986). The dividing line of alkaline and sub-alkaline is from Irvine and Baragar (1971). The data are plotted as the total 100 wt%. The triangles and circles show the whole-rock and quenched-glass compositions, respectively. The compositions of the NW Pacific petit-spots are represented by gray triangles (Hirano and Machida, 2022). The data of the 6K#1203 and 1206 basalts are from Hirano et al. (2019), and those of the 6K#1466R7 basalts are from Mikuni et al. (2022). (b) K₂O vs. Na₂O diagram. The maximum K₂O/Na₂O value of kimberlite is from PetDB database (https://search.earthchem.org/). The data of OIB and MORB are compiled from Stracke et al. (2022) as "Expert datasets" in GEOROC database (https://georoc.eu/georoc/new-start.asp).

453
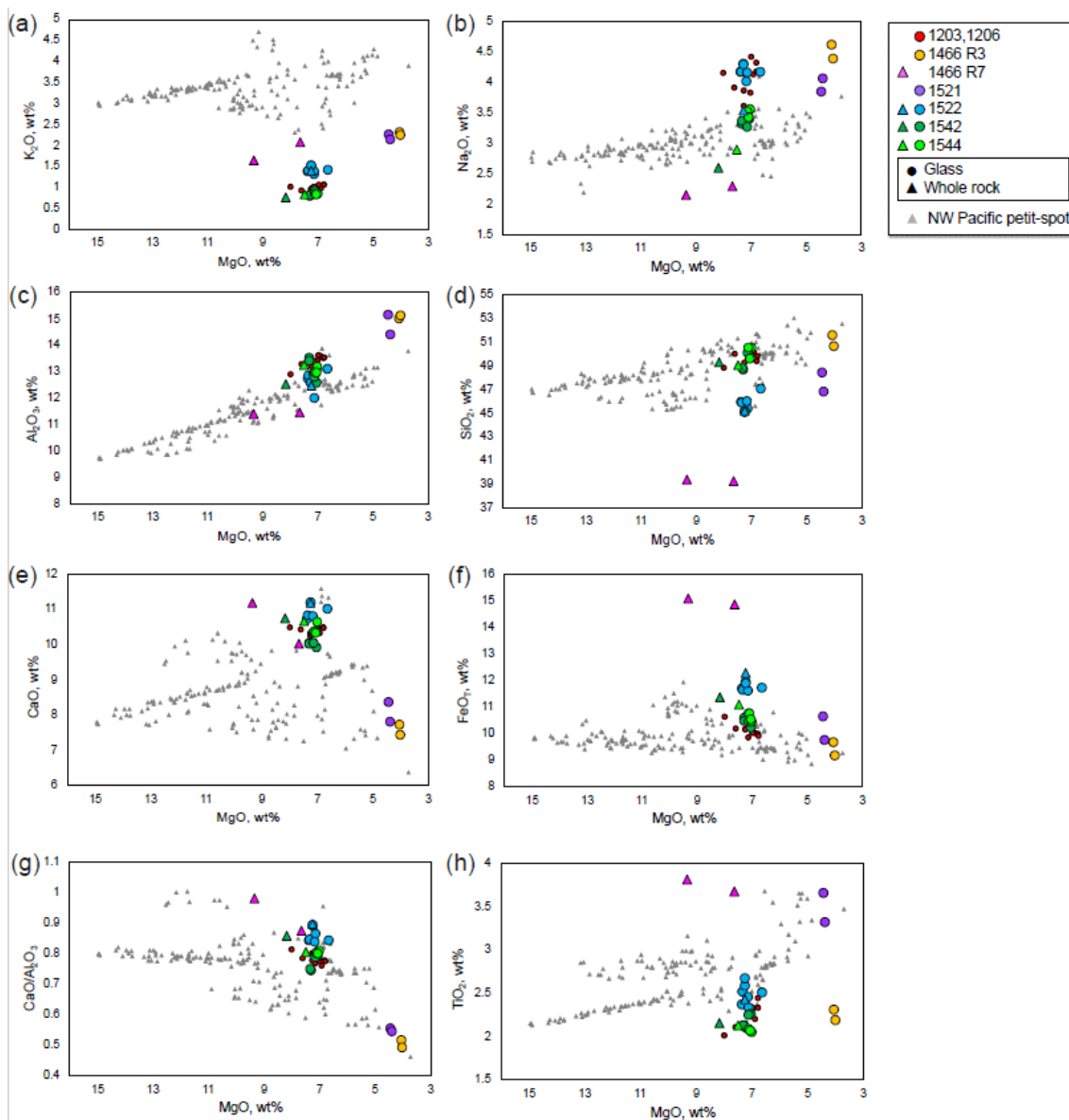
Fig. 5. Selected major-element oxides against MgO. The symbols and compiled data correspond to those in Fig. 3.

454

455

456
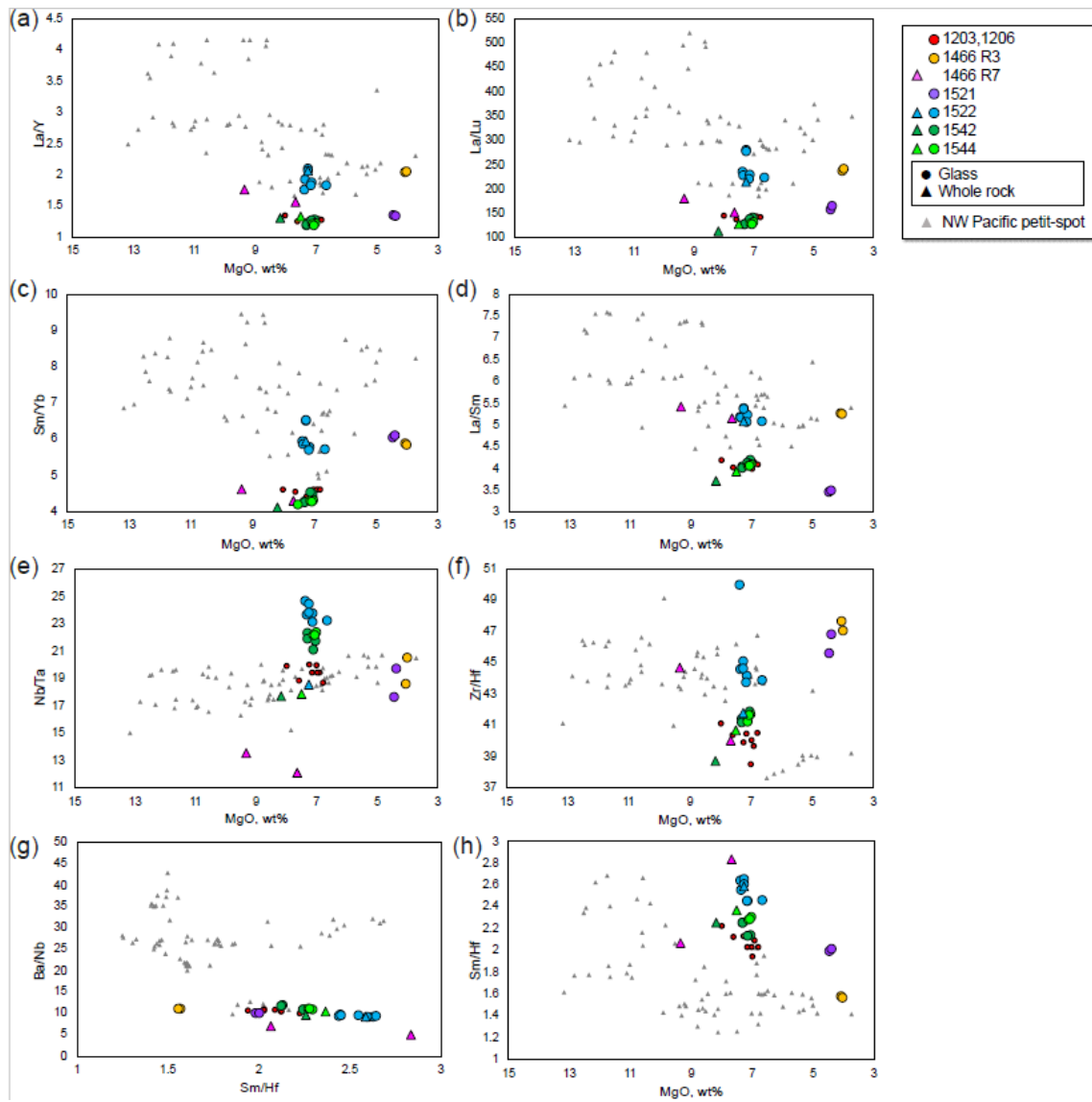
457 Fig. 6. Selected trace-element ratios against MgO. The symbols and compiled data correspond to those in Fig. 3.

458

459
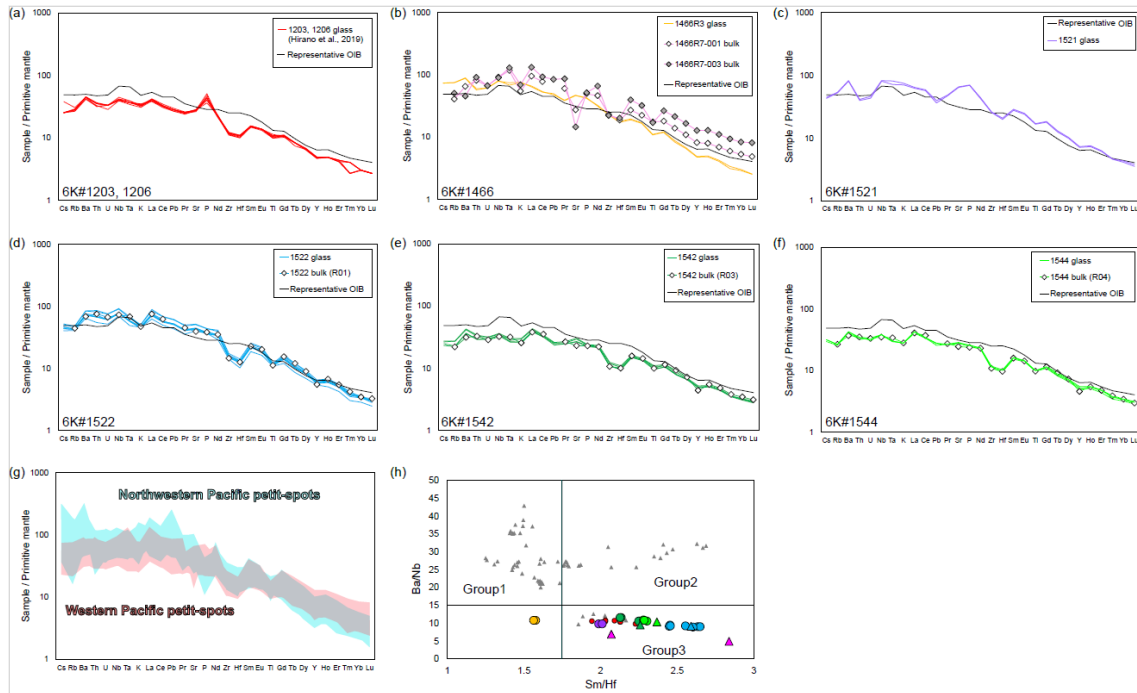
Fig. 7. Primitive mantle (PM, Sun and McDonough, 1989)-normalized trace-element patterns (a)–(g) and element ratios (h). (g) The compositional range of the study samples and NW Pacific petit-spots (Hirano and Machida, 2022). (h) The Ba/Nb and Sm/Hf ratios of the petit-spot basalts to discriminate the three groups after Machida et al. (2015). The data of 6K#1203, 1206 basalts and 6K#1466R7 basalts are from Hirano et al. (2019) and Mikuni et al. (2022), respectively. The symbols and compiled data in the (h) correspond to those in Fig. 3.

466

467
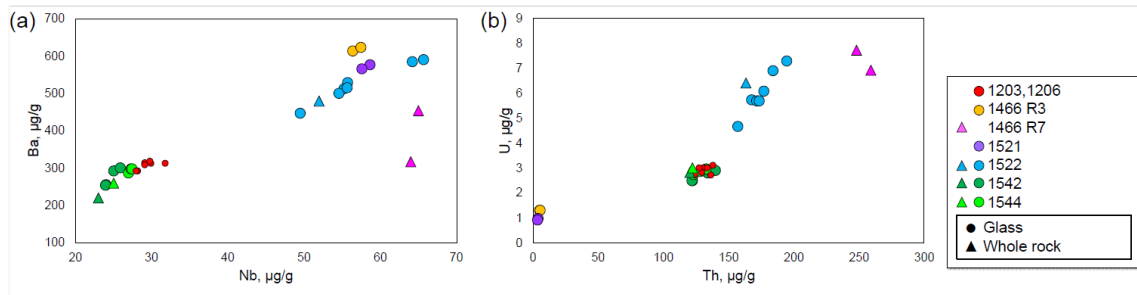
Fig. 8. Alteration sensitive elements (Ba and U) vs. insensitive elements (Nb and Th). The symbols and compiled data correspond to those in Fig. 3.

470

471

5.2 Sr–Nd–Pb isotopic composition

473

474   The Sr, Nd, and Pb isotopic compositions of the leached, unleached whole rock, and fresh glasses

475   in this study (presented in Table 4) were in practically identical ranges of $^{87}Sr/^{86}Sr$ (0.703412–

476   0.704424), $^{143}Nd/^{144}Nd$ (0.512694–0.512890), $^{206}Pb/^{204}Pb$ (18.6582–18.7778), $^{207}Pb/^{204}Pb$ (15.5086–

477   15.5749), and $^{208}Pb/^{204}Pb$ (38.6506–38.8041) despite their different locations (Figs. 9a–d, Table 4).

478   The isotopic compositions of the quenched glass and whole rock were identical, indicating that the

479   characteristics of the melting source could be obtained through the geochemistry of the young and

480   fresh volcanic quenched glass. The leached and unleached materials of the same sample also had

481   similar isotopic ratios, except for the 1466R7-003 basalt, which had a relatively high LOI (6.29 wt%)

482   (Figs. 9a–d). The Sr–Nd–Pb isotopic three-dimensional (3D) plot is shown in Fig. 9e.

483
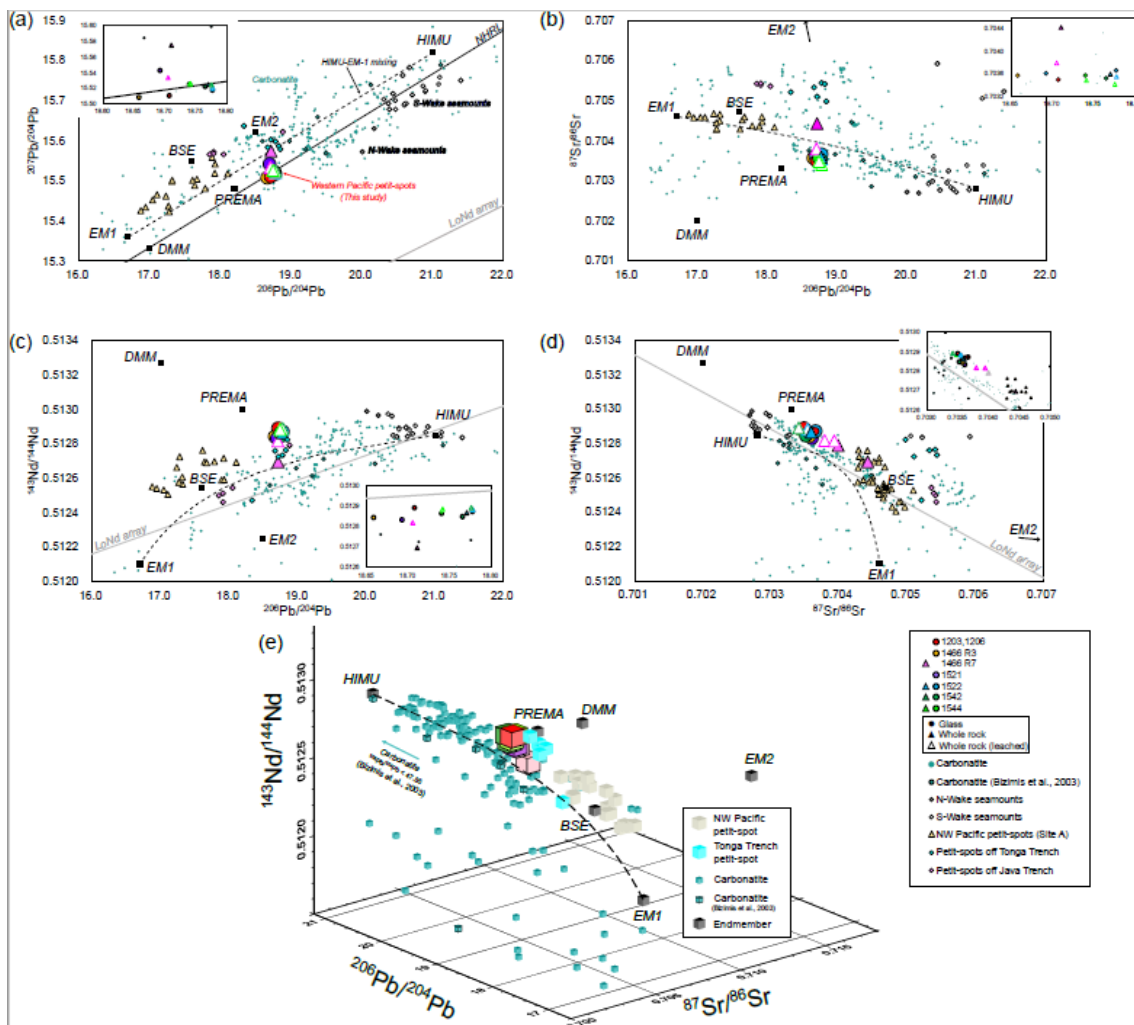
485   Fig. 9. Sr–Nd–Pb isotopic variations of the petit-spot basalts. The mantle endmembers are derived from a study by

486   Zindler and Hart (1986). The open triangles in (a)–(d) represent the acid-leached samples. Carbonatite

487   data were compiled from GEOROC (https://georoc.eu/georoc/new-start.asp) with Bizimis et al. (2003).

488   Carbonatite data with $^{87}Sr/^{86}Sr$ > 0.706 by GEOROC were eliminated. The northwestern (NW) Pacific

489   petit-spots and petit-spots off the Tonga Trench are from Hirano and Machida (2022) and Reinhard et al.

490 (2019), respectively. The petit-spots off the Java trench are from Taneja et al. (2016) and Falloon et al.

491 (2022). The data of the Wake seamounts are from studies by Konovalov and Martynov (1992), Koppers et

492 al. (2003), Konter et al. (2008), Natland (1976), Smith et al. (1989), and Staudigel et al. (1991). The

493 northern hemisphere reference line (NHRL) and Low Nd (LoNd) arrays are from studies by Hart (1984)

494 and Hart et al. (1986), respectively. (e) The three-dimensional (3D) plot of the Sr–Nd–Pb isotopic

495 compositions. The compilation and mantle endmembers correspond to (a)–(d). The color usages of the

496 plots were the same as (a)–(d).

497

Table. 4

Sr, Nd, and Pb isotopic compositions of western Pacific petit-spot basalts and measured standards.

Cruise	Sample name	Sample type	$^{87}Sr/^{86}Sr$	$^{143}Nd/^{144}Nd$	$^{206}Pb/^{204}Pb$	$^{207}Pb/^{204}Pb$	$^{208}Pb/^{204}Pb$
YK16-01	6K#1466 R3-004	Glass	0.703568 (06)	0.512842 (05)	18.6582 (07)	15.5086 (06)	38.6506 (19)
YK16-01	6K#1466 R7-001	Whole rock leached	0.703790 (05)	0.512817 (07)	18.7054 (20)	15.5337 (20)	38.8041 (50)
YK16-01	6K#1466 R7-001	Whole rock unleached	0.703989 (05)	0.512790 (06)			
YK16-01	6K#1466 R7-003	Whole rock leached	0.703933 (11)	0.512815 (05)			
YK16-01	6K#1466 R7-003	Whole rock unleached	0.704424 (05)	0.512694 (05)	18.7107 (06)	15.5749 (06)	38.7618 (17)
YK18-08	6K#1521 R04	Glass	0.703605 (05)	0.512832 (04)	18.6924 (06)	15.5428 (06)	38.7005 (19)
YK18-08	6K#1522 R01	Whole rock leached	0.703544 (05)	0.512881 (06)	18.7778 (09)	15.5209 (08)	38.7991 (22)
YK18-08	6K#1522 R01	Whole rock unleached	0.703590 (05)	0.512866 (06)	18.7705 (07)	15.5248 (07)	38.7905 (22)
YK18-08	6K#1522 R01	Glass	0.703656 (06)	0.512872 (04)	18.7773 (08)	15.5178 (07)	38.7904 (21)
YK19-05S	6K#1542 R03	Whole rock leached	0.703412 (07)	0.512890 (06)	18.7759 (10)	15.5244 (11)	38.7574 (36)
YK19-05S	6K#1542 R05	Glass	0.703517 (06)	0.512847 (04)	18.7653 (08)	15.5224 (07)	38.7345 (19)
YK19-05S	6K#1544 R04	Whole rock leached	0.703480 (04)	0.512883 (05)	18.7413 (14)	15.5262 (14)	38.745 (41)
YK19-05S	6K#1544 R04	Glass	0.703568 (05)	0.512863 (04)	18.7400 (08)	15.5253 (09)	38.7347 (22)
YK10-05	6K#1206 R04	Glass	0.703492 (05)	0.512890 (04)	18.7074 (06)	15.5109 (07)	38.6970 (19)
YK10-05	6K#1206 R04 duplicate	Glass			18.7071 (07)	15.5119 (07)	38.6950 (18)

Type of value	Standared for each isotope		$^{87}Sr/^{86}Sr$	$^{143}Nd/^{144}Nd$	$^{206}Pb/^{204}Pb$	$^{207}Pb/^{204}Pb$	$^{208}Pb/^{204}Pb$
Analyzed value	JB-2		0.703721 (05)	0.513094 (04)	18.3326 (05)	15.5453 (06)	38.2240 (17)
Reference value	JB-2	Sr, Nd: Orihashi et al. (1998), Pb: Tanimizu and Ishikawa (2006)	0.703709 (29)	0.513085 (08)	18.3315 (25)	15.5460 (21)	38.2240 (55)
Analyzed value	JNdi-1	(n=2)		0.512103 (05)			
Reference value	JNdi-1	Wakaki et al. (2007)		0.512101 (11)			
Analyzed value	SRM987	(n=2)	0.710239 (05)				
Reference value	SRM987	Weis et al. (2006)	0.710254 (02)				
Analyzed value	SRM981				16.9303 (05)	15.4828 (06)	36.6710 (16)
Reference value	SRM981	Tanimizu and Ishikawa (2006)			16.9308 (10)	15.4839 (11)	36.6743 (30)

498 Errors shown in parentheses represent 2σ and apply to the last two digits.

499

5.3 Age determination and estimation

501

502 The $^{40}Ar/^{39}Ar$ ages were determined for two samples (1466R6-001 and 1522R01) (Fig. 10a,

503 Table S4). The secondary material (e.g., alteration products) plausibly causes the recoil loss and

504 redistribution of Ar during irradiation of samples, particularly fine-grained groundmass separates of

505 submarine basalt (Koppers et al., 2000). This effect is negligible for $^{40}Ar/^{39}Ar$ dating samples in this

506 study because the total K/Ca ratios estimated using the irradiated $^{39}Ar_K/^{37}Ar_{Ca}$ ratio (0.089 for

507 6K#1466R6, 0.080 for 6K#1522R01; Table S4) are mostly correspond to the bulk K/Ca ratios

508 calculated using the major element compositions of Table 2 (0.088 for 6K#1466R7-001, 0.076 for

509 6K#1522R01). This is supported by the rock descriptions recognized no secondary materials of

510 crystalline ^{40}Ar/^{39}Ar specimens. Sample 1466R6-001 had a plateau age of 3.03 ± 0.18 Ma in seven

511 fractions comprising 94.1% released ^{39}Ar. However, the plateau age was recognized as apparently old,

512 owing to excess ^{40}Ar, as indicated by the initial ^{40}Ar/^{36}Ar ratio of 325 ± 15, which exceeded the

513 atmospheric ratio (296.0; Nier, 1950) in the inverse isochron. The inverse isochron age of 2.56 ± 0.34

514 Ma showed the best age estimate for the 1466R6-001 basalt (Fig. 10a). The 1522R01 sample released

515 almost no radiogenic daughter nuclide of ^{40}Ar in the K–Ar age system (Fig. 10a).

516   The ranges of eruption age were estimated for all the samples using the average thickness (n =

517 20) of ferromanganese crust and palagonite rind (hydrated quenched glass) with their

518 deposition/formation rates on the seafloor (ferromanganese crust, 1–10 mm/Myr; Hein et al., 1999;

519 palagonite, 0.03–0.3 mm/Myr; Moore et al., 1985) (Fig. 10b). Using this approach, the western Pacific

520 petit-spots were expected to have erupted later than ca. 9 Ma. The ranges of eruption age estimated

521 from palagonite rind did not overlap with those from ferromanganese crust showing older durations,

522 although they had general correlations (Fig. 10b). The ^{40}Ar/^{39}Ar ages of two samples and the U-Pb

523 age of zircon in the 1203 and 1206 peperites (Hirano et al., 2019) were overlaid within these ranges.

524
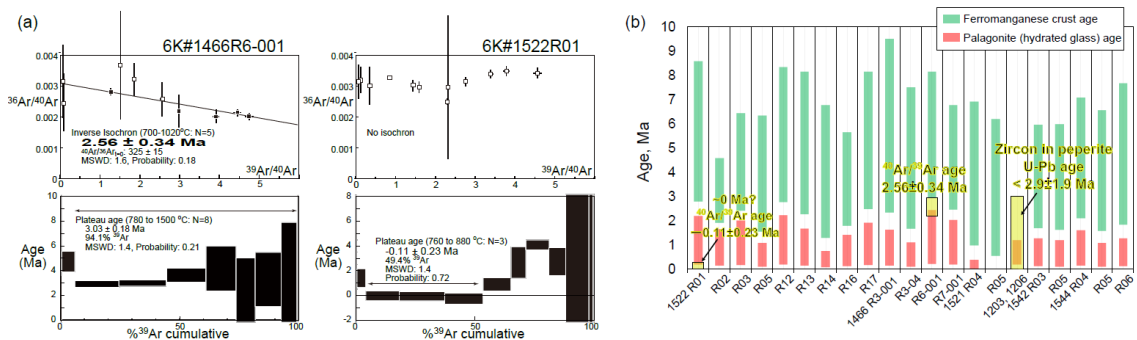
526 Fig. 10. Geochronological data. (a) The ^{40}Ar/^{39}Ar ages of the 6K#1466R6-001 and 6K#1522R01 basalts. The errors

527   show a 2-sigma confidence level. (b) Estimated relative ages using the thickness of ferromanganese crust

528   (green bands) and palagonite (hydrated quenched-glass rind; red bands) covered with petit-spot basalts.

529   These values were estimated using the average for each sample (n = 20). The U-Pb age of zircon in the

530   6K#1203 and 1206 peperites are from Hirano et al. (2019).

531

6 Discussion

533

6.1 Eruptive setting of western Pacific petit-spots

535

536   Here, two crystalline petit-spot basalts were subjected to ^{40}Ar/^{39}Ar dating. A previously reported

537 petit-spot knoll in this region (examined during the 6K#1203 and 1206 dives) aged "younger than 3

538 Ma" was investigated using the U–Pb dating of eight zircons in peperites (Fig. 10b) (Hirano et al.,

539 2019). The results showed that the silica-undersaturated vesicular basalt of 6K#1466R6-001, as a host

540 of ultramafic xenoliths (Mikuni et al., 2022), exhibited a $^{40}Ar/^{39}Ar$ age of 2.56 ± 0.34 Ma (Fig. 10).

541 Oppositely, the fresh vesicular basalt of 6K#1522R01, which erupted at the foot of the 100-Ma

542 Takuyo-Daigo seamount (Fig. 2) (Nozaki et al., 2016), did not exhibit radiogenic ^{40}Ar highlighting

543 that this sample is quite young (approximately 0 Ma) (Fig. 10). The ranges of eruption ages were

544 estimated using the average thickness of ferromanganese crust and palagonite rind (seawater-hydrated

545 quenched glass) with their deposition/formation rates on the seafloor. The $^{40}Ar/^{39}Ar$ and zircon U–Pb

546 ages were within these ranges (Fig. 10). Here, the petit-spot volcanic field is surrounded by Cretaceous

547 seamounts (Koppers et al., 2003) and irregular Paleogene volcanoes (Aftabuzzaman et al., 2021;

548 Hirano et al., 2021). However, no zero-aged hotspots were observed in this region, and the P-wave

549 tomographic image of the surface to the core–mantle boundary of the study area did not exhibit a

550 plume-like low-velocity zone (Fig. 1c; Lu et al., 2019). Furthermore, the MORB-like to more depleted

551 noble-gas isotopic compositions of the petit-spot knoll (6K#1203, 1206) suggested its upper mantle

552 origin (Yamamoto et al., 2018). Along with the outer-rise bulge in front of the Mariana Trench detected

553 through a positive gravitational anomaly (Hirano et al., 2019), these data suggest that the western

554 Pacific petit-spot volcanoes could have erupted at ~0–3 Ma owing to the flexure of the subducting

555 Pacific Plate into the Mariana and Ogasawara Trenches.

556   The petit-spot basalts from the 6K#1542 and 1544 dives could have originated from the same

557 eruptive source based on their similar petrographic and geochemical features despite a distance of

558 approximately 6.8 km between both (Figs. 3d, 4, 5, 6, 7, 8, and 9). Contrarily, in terms of their

559 petrography and geochemistry, the basalts from the 6K#1466 dive are discriminated between the

560 samples from the lava flows on the abyssal plain (R3-001 and R3-004) and the samples from the knoll

561 site (R6-001, R7-001, and R7-003). The R3 basalts were collected at a lava outcrop 600 m south of

562 the knoll, and the R6 and R7 samples were collected on the western slope of the knoll (Fig. 3a). The

563 6K#1466R3 series are glassy with a high SiO_2 content (50.6–51.6 wt%), including minor plagioclase

564 and less vesicles (Figs. 3a and 4a). However, the 6K#1466R6 and R7 series exhibited silica-

565 undersaturated compositions (SiO_2 = 39.3–39.4 wt%) and high vesicularities (20–40 vol.%) (Figs. 3b

566 and 4a). Combining these observations with the differences in MgO contents and trace element

567 compositions, the R3 and R6–R7 basalts are implied to have different parental magmas (Figs. 6 and

568 7b). Generally, vesicular samples (6K#1203, 1206, 1466R7, 1522, 1542, and 1544 basalts) are

569 relatively primary (i.e., MgO > 6.63 wt%), whereas nonvesicular samples (6K#1466R3 and 1521

570 basalts) are evolved (i.e., MgO < 4.43 wt%). This correlates with the compositions of olivine

571 microphenocrysts in the low forsterite content (Fo# = $100 \times Mg/[Mg+Fe^{2+}]_{cation}$) of olivine in evolved

572 basalts and the high Fo# of olivine in the relatively primary basalts (Figs. S1a–c).

573   The CI chondrite-normalized REE ratios of these samples are within those of OIBs, and the

574 REE patterns exhibit HREE-depleted patterns (Fig. S3). However, among the western Pacific petit-

575 spots, the REE and trace element ratios differ for each volcano (i.e., parental magmas) (Figs. 6 and

576 S3). Given the lack of correlation between MgO and the trace element ratios, each volcano could have

577 originated from isolated sources (i.e., melt ponds) with different chemical compositions and degrees

578 of melting (Fig.6). Oppositely, the radiogenic Sr, Nd, and Pb isotopic ratios of the samples are nearly

579 identical, and the components in the source are probably equivalent (Fig. 9).

580 Summarily, (1) the western Pacific petit-spot volcanoes erupted at ~0–3 Ma owing to the plate

581 flexure related to the subduction of the Pacific Plate into the Mariana Trench (Figs. 1 and 2). (2) The

582 6K#1542 and 1544 samples originated during the same magmatic event (Fig. 3d). However, the basalts

583 from the 6K#1466 dive are subdivided into two parental magmas (R3 and R6–R7 basalts) (Fig. 3a).

584 (3) Each volcano originated from isolated source and/or ascending processes based on the independent

585 trace element ratios. The geochemical components involved in the source, however, were similar

586 among the western Pacific petit-spot volcanoes because of the nearly identical Sr, Nd, and Pb isotopic

587 compositions (Figs. 6 and 9). A variation in the trace element compositions among the volcanoes is

588 plausibly due to the degree of contribution of carbonatite flux and/or the recycled crustal component

589 to the source, as discussed below.

590

591 **6.2 Petit-spot magma composition and its evaluation**

592

593 Post-eruption seawater alteration might have affected the chemical composition of oceanic

594 basalts. Thus, various approaches, including petrographic observation, geochemical investigation, and

595 acid leaching, have been employed to evaluate the primary features and the removal of this effect for

596 isotopic analysis (Hanano et al., 2009; Melson et al., 1968; Miyashiro et al., 1971; Nobre Silva et al.,

597 2009; Resing and Sansone, 1999; Staudigel and Hart, 1983; Zakharov et al., 2021). The study samples

598 exhibit whole-rock LOI <1.72 wt%, excluding two relatively altered samples, 6K#1466R7-001 (LOI

599 = 2.68 wt%) and R7-003 (LOI = 6.29 wt%). Pristine quenched glasses are preserved in most of the

600 samples, excluding three exceptional samples (the 6K#1466R6-001, R7-001, and R7-003 basalts).

601 Positive correlations are observed between the alteration-insensitive (e.g., Nb, Th) and -sensitive (e.g.,

602 Ba, U) incompatible elements. This indicates that the effect of seawater alteration was not extensive,

603 excluding the 6K#1466R7-001 and R7-003 basalts (Fig. 8). Although each sample was derived from

604 different volcanic edifices, the positive correlation of all the study samples is due to the chemical

605 similarity of the source compositions for certain elements (i.e., Ba/Nb and U/Th ratios are nearly

606 constant among the samples), as well as the Sr, Nd, and Pb isotopic compositions (Fig. 9). These

607 observations showed that most of the petit-spot basalts were unaffected by seawater alteration with a

608 few exceptions (i.e., 1466R7-001 and R7-003 basalts).

609 The variable MgO (4–9 wt%), Ni (<263 ppm), and Cr (<350 ppm) contents in the samples are

610 lower than the expected values of primary mantle-derived melt (MgO >10 wt%, Ni >400 ppm, Cr

611 >1000 ppm; Frey et al., 1978). Similarly, the Mg# ($100 \times Mg/[Fe^{2+} + Mg]_{molar}$) values are differentiated

612 in the range of 41–57 (Table 2) against the primary basaltic melt, which is equilibrated with the upper

613 mantle (Mg# = 66–75; Irving and Green, 1976). No phenocrysts were observed (only

614 microphenocryst), despite such differentiated compositions as well as most of the NW Pacific petit-

615 spot basalts. This suggests that the western Pacific petit-spots experienced crystal fractionation in the

616 lithosphere as well as the case of NW Pacific petit-spot (Machida et al., 2017; Valentine and Hirano,

617 2010; Hirano, 2011; Yamamoto et al., 2014). Therefore, the calculation of primary composition of the

618 petit-spot basalts using the mineral modal composition on the thin section could not be performed.

619 However, the trends of the major elements of the samples imply the crystal fractionation of the same

620 phases. The negative trends of the Al_2O_3 content and the positive trends of the CaO and CaO/Al_2O_3

621 content with a decrease in MgO indicate the occurrence of olivine, spinel, and clinopyroxene

622 fractionation (Figs. 5c, e, and g). The absence of visible correlations of the K_2O, Na_2O, SiO_2, and TiO_2

623 contents against MgO suggests that the fractionation of plagioclase and the Fe–Ti oxides was

624 insignificant. The Fe–Ti oxides as minor phases in the groundmasses and plagioclases were only

625 observed in the most differentiated 1466R3-001 and R3-004 basalts (Figs. 3, 5a, b, d, and h). However,

626 these major elemental trends should be interpreted as apparent trends because each petit-spot volcano

627 originated from an isolated parental magma with different chemical composition or degree of partial

628 melting as discussed above.

629   The trace element composition of alkali basalts can be used to determine the melting source

630 rather than major elements (Hofmann, 2003; Machida et al., 2014, 2015). Trace element composition

631 of magma, however, could be modified by crustal and/or mantle assimilation and fractionation of

632 certain minerals. The relatively primitive basalts (6K#1203, 1206, 1466R6, R7, 1522, 1542, and 1544)

633 included xenocrystic olivines and partly ultramafic xenoliths, indicating a rapid magma ascent (Hirano

634 et al., 2019; Mikuni et al., 2022; Fig. S4). However, since the stagnation of ascending petit-spot magma

635 could occur to create fertile peridotite and pyroxene-rich veins from the middle to lower depths of the

636 lithosphere (Mikuni et al., 2022; Pilet et al., 2016), the chemical composition of the petit-spot magma

637 could be modified because of assimilation with the ambient lithospheric peridotite. According to

638 Hirano and Machida (2022), ascending silica-undersaturated melt would mainly consume

639 orthopyroxene (±spinel) and become a more silicic composition with Zr and Hf depletion. This is

640 because of the relatively higher Zr–Hf partition of orthopyroxene than those of other trace elements

641 (Pilet et al., 2008; Shaw, 1999; Tamura et al., 2019). The orthopyroxenes of fertile pyroxenites and

642 lherzolite xenoliths metasomatized by petit-spot melts exhibit Zr and Hf enrichment (Mikuni et al.,

643 2022; Fig. S5). If this silica-enrichment (i.e., melt–rock interaction) was significant, a positive

644 correlation between SiO_2 and Sm/Hf is expected as a mantle assimilation trend. However, the samples

645 exhibit a negative correlation, similar to those of the NW Pacific petit-spots (Hirano and Machida,

646 2022) (Fig. S2). Considering the relationship between the Sm and Hf partition coefficients of

647 clinopyroxene (i.e., $D^{Hf} < D^{Sm}$; McKenzie and O'Nions, 1991; Kelemen et al., 2003), we suggest that

648 the negative correlation between the Sm/Hf and SiO$_2$ of the petit-spot basalts probably reflects the

649 crystal fractionation of clinopyroxene rather than mantle assimilation. The Ba/Nb ratios of the samples

650 are nearly constant and do not correlate with the MgO and SiO$_2$ contents (Figs. 6g and S2g). The lack

651 of correlation between the other trace element ratios, excluding Sm/Hf and Ba/Nb (i.e., La/Y, La/Lu,

652 Sm/Yb, La/Sm, Nb/Ta, Zr/Hf), and the MgO concentration imply that crystal fractionation may not

653 have been involved with those of the incipient melt (Fig. 6). However, it is difficult to independently

654 follow the evolution of the trace element composition for each volcano since each volcano originated

655 from isolated sources. Thus, considering the observations above, the fresh and zero-aged 6K#1522

656 basalts (the highest Sm/Hf ratios and lowest SiO$_2$ contents among the fresh samples and higher MgO

657 contents) were selected for further analysis with geochemical modeling. Considering that the 6K#1522

658 samples had MgO in the range of 6.63–7.36 wt%, olivine was expectedly the dominant phase of crystal

659 fractionation (Asimow and Langmuir, 2003; Helz and Thornber, 1987; Herzberg, 2006). When the

660 olivine maximum fractionation model (Takahashi et al., 1986; Tatsumi et al., 1983) was applied to test

661 two samples, the calculated primary trace element contents did not significantly differ from those of

662 the analytical compositions (Table S5 and Fig. S6). Thus, the 6K#1522 basalts were assumed to be the

663 most primary petit-spot basalt samples and were used to evaluate the geochemical modeling results.

664

665 **6.3 Melting source of western Pacific petit-spots**

666

667 The depletions of specific elements (e.g., Ta, Zr, Hf, and Ti) of petit-spot basalts potentially

668 demonstrate the involvement of carbonatitic materials in conjunction with a large amount of CO$_2$ and

669 lower Mg isotopic ratio than that of the normal mantle (Bizimis et al., 2003; Dasgupta et al., 2009;

670 Hirano and Machida, 2022; Hoernle et al., 2002; Liu et al., 2020; Okumura and Hirano, 2013). Other

671 oceanic lavas originating from the asthenosphere (e.g., Hawaiian rejuvenated lavas and North Arch

672 volcanoes) exhibited characteristic trace element signatures (i.e., Zr and Hf depletion) similar to those

673 of petit-spot lavas. This implies that their melting sources were involved with carbonatitic materials

674 with or without plume-derived components (Fig. S7; Borisova and Tilhac, 2021; Clague and Frey,

675 1982; Clague et al., 1990; Dixon et al., 2008; Yang et al., 2003). In addition, the involvement of

676 recycled crustal components was inferred from the geochemical features of the petit-spot basalts, and

677 the upper mantle was revealed to be heterogeneous (Liu et al., 2020; Machida et al., 2009, 2015). Such

678 scenario of the source on petit-spot magma is consistent with the previously suggested petrogenesis

679 of alkaline rocks explained by the addition of CO$_2$-rich components and/or recycled crustal materials

680 with or without sediment to the mantle (e.g., Dasgupta et al. 2007; Hofmann, 1997). Conversely, the

681 melting of an amphibole-rich metasomatic vein explains the major and trace element composition of

682 alkali basalts (Pilet et al., 2008; Pilet, 2015). However, the experimentally produced melts exhibit Pb

683   depletion and a positive Nb-Ti anomaly in the PM-normalized trace element patterns (Fig. S8)

684   inconsistent with the petit-spot basalts (Fig. 7). In addition, Juriček and Keppler (2023) demonstrated

685   that amphibole dehydration is not the cause for the oceanic LAB by high-pressure experiment on the

686   realistic condition. The fertile pyroxenitic xenoliths and pyroxene xenocrysts occurring in the 1466R6

687   and R7 basalts, which originated from the metasomatic vein related to prior petit-spot magmatism,

688   had neither amphiboles nor other hydrous minerals (Mikuni et al., 2022).

689   To discuss the involvement of carbonatitic and crustal components in petit-spot melts, a partial

690   melting model of the heterogeneous mantle is provided. The involvement of carbonatitic fluids and

691   recycled materials in the genesis of petit-spot melts has been suggested, and the open-system model

692   with carbonatite influx from the outer system was employed using "OSM-4" of Ozawa (2001),

693   referring the parameters of Borisova and Tilhac (2021). This model is based on the mass conservation

694   equations of one-dimensional steady-state melting. In this present study, the model uses a critical melt

695   fraction (α_c; mass fraction of melt when melt separation begins = melt connectivity threshold) at 0.005

696   or 0.01. The system is opened to fluxing at a constant melt-separation rate (γ) when the system reaches

697   the α_c. The final trapped melt fraction (α_f; mass fraction of melt trapped in the residue) was fixed at ~0

698   (it was calculated as 10^{-6} owing to mass balance). We calculated the trace element composition of

699   partial melts at various degree of melting (F), a few rates of influx (β) and melt separation (γ). We

700   assumed a primitive mantle (PM) source as a lherzolite with or without a normal (N)-MORB source

701   as the recycled oceanic crust (Sun and McDonough, 1989), such as pyroxenite and eclogite. The

702   recycled crust (N-MORB component) was mixed in the source as compositional heterogeneity

703   calculated as "0.05N-MORB + 0.95PM" for the trace element concentration, and the considered

704   mineral phases and their proportions were derived only from garnet lherzolite (i.e., olivine,

705   orthopyroxene, clinopyroxene, and garnet). The mineral mode of garnet lherzolite (olivine 55%,

706   orthopyroxene 20%, clinopyroxene 15%, and garnet 10%) and the melting reaction mode (olivine 8%,

707   orthopyroxene −19%, clinopyroxene 81%, and garnet 30%) are based on studies by Johnson et al.

708   (1990) and Walter (1998), respectively. The proportion of olivine and garnet was also changed to

709   evaluate the effect of garnet modal ratio to the produced melt composition. In this situation, the

710   clinopyroxene is consumed at an F (degree of partial melting) of ~ 19%; therefore, the system was

711   calculated up to 18% partial melting. The carbonatite melt, as an influx, in this model is "average

712   carbonatite" from a study by Bizimis et al. (2003). The partition coefficient of trace elements is

713   generally based on a study by McKenzie and O'Nions (1991, 1995) excluding Ti for clinopyroxene

714   and garnet (Kelemen et al., 2003). The variables of β (influx rate) and γ (melt-separation rate) were

715   changed during the modeling within the mass balance ($\gamma \leqq \beta + 1$). The modeled melts were outputted

716   as "total melt," considering the instantaneous and accumulated melts. For the carbonatite composition,

717   the value of "average carbonatite" of Bizimis et al. (2003) is applied because the chemical composition

718   of carbonatite is largely diverse, and this value is recommended for geochemical modeling (Bizimis

719   et al., 2003). The parameters are listed in Table S6. As a result, partial melting of garnet lherzolite with
720   10% carbonatite influx to a given mass of source (i.e., garnet lherzolite) can roughly explain the trace
721   element pattern of petit spot basalts (Figs. 11a–e), and the presence of 5% crustal component in the
722   source is the most plausible model of petit-spot magma generation (Figs. 11b and d). In addition,
723   slightly less garnet in the lherzolite source than the modal ratio of Johnson et al. (1990) fits the petit-
724   spot better (Fig. 11b). In both cases, the presence of a crustal component in the source yields more
725   plausible results (Figs. 11a–d). The higher carbonatite influx (β =1.0) could not explain the trace
726   element composition of the petit-spot basalts (Fig. 11f). The melt connectivity threshold (α_c) of 0.01
727   is plausible because higher connectivity of melt (i.e., lower α_c value) leads to enrichment of LILEs and
728   LREEs (Fig. 11g). The results also showed that the melt-separation ratio is insignificant to the trace
729   element composition of the calculated melts (Figs. 11d and e). Thereafter, we concluded that the partial
730   melting of ~5% crustal component-bearing garnet lherzolite with ~10% carbonatite flux to a given
731   mass of the source plausibly explains the melting source of petit-spot volcanoes (Figs. 11b and d).
732   Assuming that the trace element composition of 6K#1203, 1206, 1542, and 1544 basalts are also
733   primitive, they may be explained by a partial melting of garnet lherzolite with 5% crustal component
734   and lower carbonatite influx rate (β = 0.03) (Fig. S9). Actually, the 6K#1203, 1206, 1542, and 1544
735   basalts exhibited the similar MgO contents and Mg# to those of 6K#1522 basalts (Fig. 4 and Table 2).
736   These results provide quantitative evidence on the petrogenesis of petit-spots, i.e., the contribution of
737   carbonatite melt and recycled oceanic crust.
738   Although the melting source contained small proportions of carbonatite melt and crustal
739   components, these components could have contributed to the isotopic composition because of their
740   abundant incompatible elements rather than the ambient mantle. The determination of the Sr, Nd, and
741   Pb isotopic compositions revealed that they had geochemically identical prevalent mantle (PREMA)-
742   like sources (Fig. 9). They do not belong to any mantle isotopic endmembers (i.e., depleted MORB
743   mantle (DMM); EM-1, -2; and HIMU; Fig. 9) contrary to those of NW Pacific petit-spots toward the
744   EM-1 isotopic composition (Machida et al., 2009; Liu et al., 2020). In the Pb isotopic space, the present
745   samples do not correlate with those of the neighboring HIMU-like Cretaceous seamounts (Fig. 9a) (N-
746   Wake, S-Wake seamounts; Konter et al., 2008; Koppers et al., 2003; Natland, 1976; Smith et al., 1989;
747   Staudigel et al., 1991). For the melting source of the NW Pacific petit-spot basalts, the contributions
748   of the eclogite/pyroxenite endmember as recycled oceanic crust and the carbonated endmember were
749   suggested based on the major and trace elements and the Mg, Sr, Nd, and Pb isotopic compositions
750   with the Mg diffusion modeling (Liu et al., 2020). The higher FeO/MnO ratios of the present melts
751   (65.9–78.0), compared with those of partial melts originating from peridotite (50–60), are attributed
752   to the presence of recycled pyroxenite (Herzberg, 2011). This could have contributed to the crustal
753   components in the melting source. However, the western Pacific petit-spots in this study identically
754   exhibited a PREMA-like isotopic signature without extreme endmember contributions as described

755   above (Fig. 9). Such isotopic compositions with the world's petit-spots can be possibly explained by

756   the diverse mixing proportion of HIMU and EM-1 components (Fig, 9e). The isotopic compositions

757   of the NW Pacific petit-spots (off the Japan Trench), Samoan petit-spots (off the Tonga Trench), petit-

758   spot dikes in Christmas Island (off the Java trench), and western Pacific petit-spots (off the Mariana

759   Trench in this study) are roughly along the HIMU–EM-1 mixing line (Fig. 9e). Furthermore, the

760   isotopic compositions of global carbonatites can be generally explained by the mixing of HIMU and

761   EM-1 (Bell and Tilton, 2002; Hoernle et al., 2002; Hulett et al., 2016). The contributions of the

762   carbonated material/carbonatite and crustal components to the melting source were suggested in terms

763   of the origin of HIMU and EM-1 (Collerson et al., 2010; Hanyu et al., 2011; Wang et al., 2018; Weiss

764   et al., 2016; Workman et al., 2004; Zindler and Hart, 1986). However, the EM-1 and HIMU

765   components could not be determined to be carbonated component and recycled crust, respectively,

766   owing to the various views on each tectonic setting for the mantle endmember. The variability of global

767   carbonatite isotopic compositions also makes it difficult to determine their representative isotope ratios

768   (Fig. 9). Although such issues make a quantitative isotopic mixing model challenging, the HIMU-EM-

769   1 like trend of the global petit-spot volcanoes may reflect the involvement of carbonatitic and recycled

770   crustal materials. Conclusively, the mass balance models on the trace elements and the isotopic

771   variations in the petit-spot volcanoes confirmed the contribution of carbonatite melt and the recycled

772   oceanic crust to the melting source of the western Pacific petit-spots (Fig. 12). Experimental studies

773   have revealed the various petrogenesis of carbonatite and carbonatitic alkali-rich magma under high

774   pressures (Dasgupta et al., 2006; Ghosh et al., 2009). The geochemistry of petit-spot basalts including

775   Mg isotopes suggested that the conceivable origin of carbonatite related to the petit-spot melt is

776   subducted "carbonated" pelite, pyroxenite/eclogite, or peridotite stored as diamond or metal carbide

777   in the reduced lower portion of the upper mantle (Liu et al., 2020; Rohrbach et al., 2007). Subducted

778   carbonated pelite, for example, would melt under high pressure (>8 GPa) through the oxidation at the

779   redox boundary where the the iron–wüstite (IW) buffer changes to the quartz–fayalite–magnetite

780   (QFM) buffer (i.e., redox melting; Grassi and Schmidt, 2011). Chen et al. (2022) demonstrated that

781   the alkali-rich carbonatite melt could occur under a pressure higher than 6 GPa, particularly exhibiting

782   K-rich and Na-rich carbonatites under 6–12 and >12 GPa, respectively. This pressure-dependent

783   alkalinity of the produced carbonatite melts might explain the variation between potassic NW Pacific

784   petit-spot lavas and present sodic petit-spot lavas (Fig. 4b). On the other hand, an experimental study

785   pointed out the existence of carbonate-rich layer in the LAB owing to the horizontally spread carbonate

786   from around the wedge mantle rather than upwelling from the deep mantle (Hammouda et al., 2020).

787   Several high pressure–temperature experiments and modeling revealed that the chemical composition

788   of intraplate magmas from upper mantle depends on their original depth; carbonatitic melt can be

789   generated beneath thick cratonic lithosphere (~250–200 km), kimberlitic melt would be produced at

790   >120 km in depth, and alkali basalt would occur at 100–60 km in depth by partial melting of "original"

791 CO$_2$ and H$_2$O-bearing mantle (Massuyeau et al., 2021). These depth-dependent compositional

792 variation, that is, K-rich kimberlite to alkali basalt may also explain the geochemical gap between K-

793 rich NW Pacific petit-spots and K-poor western Pacific petit-spots (Fig. 4b). Although the multiple

794 origins of carbonatite are merely suggested and remain unclear, carbon-rich components play a key

795 role in the partial melting of mantle at the LAB (Sifré et al., 2014), that is, the source of petit-spot

796 magma.
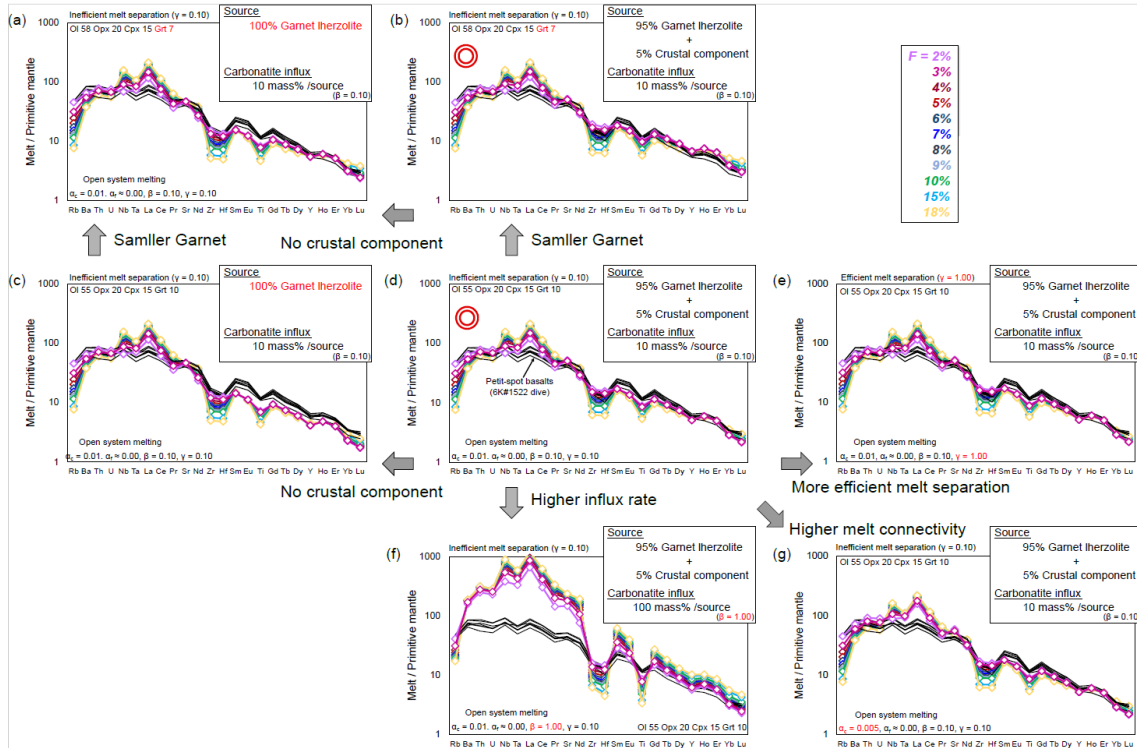
797

798 Fig. 11. Geochemical modeling for the primitive mantle (PM)-normalized trace-element pattern. The calculated

799   hypothetical melts are a production of carbonatite influx melting of garnet lherzolite with or without 5%

800   crustal component. Detailed information of the parameters is described in Section 6-3 and Table S6. F is

801   the degree of melting (%). The trace-element composition of the western Pacific petit-spot basalts from

802   the 6K#1522 dive is shown as black lines for comparison. The PM composition of lherzolite and the N-

803   MORB composition of recycled crust were based on a study by Sun and McDonough (1989). The influx

804   carbonatite is the "average carbonatite" of a study by Bizimis et al. (2003). The parameters used in the

805   open-system melting models were as follows: a_c is a critical melt fraction, a_f is a final trapped melt

806   fraction, β is a melt influx rate, and γ is a melt-separation rate. Model results are compared by varying

807   each parameter, i.e., garnet modal ratio and presence of crustal material (a–d), melt-separation rate (d and

808   e), carbonatite influx rate (d and f), and critical melt fraction (d and g). Each figure is expressed based on

809   the difference from the condition in (d).

810
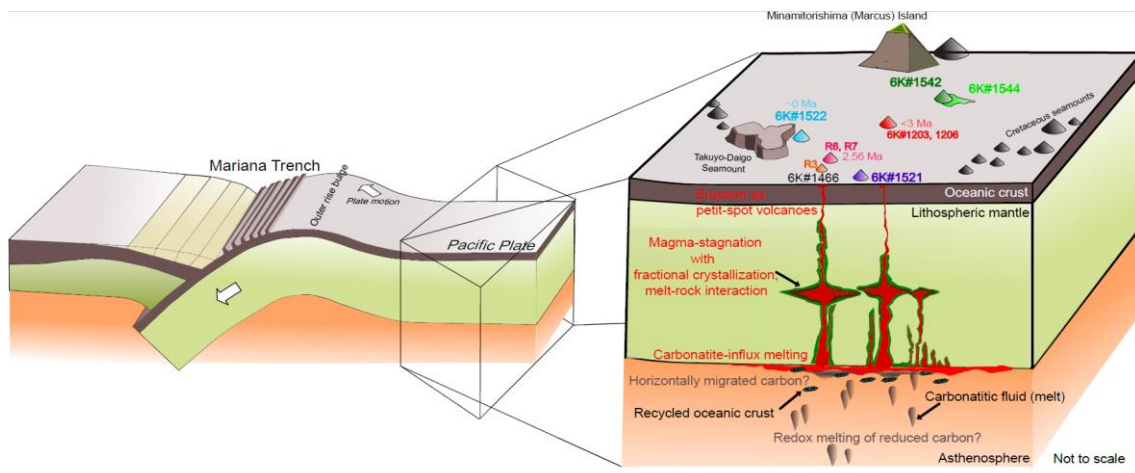
811

812 Fig. 12. Schematic illustration of the magmatic processes of the western Pacific petit-spot volcanoes.

813   Carbonatitic melt and recycled oceanic crust potentially induce partial melting of asthenospheric mantle

814   beneath the western Pacific region. Carbonatitic melt might have originated from a carbon-rich

815   component horizontally migrated from a subduction zone (Hammouda et al., 2020), or a redox melting

816   of reduced carbon in the deep mantle (Chen et al., 2022; Grassi and Schmidt, 2011; Rohrbach et al., 2007).

817   Petit-spot magma stagnated in the lithosphere with fractional crystallization and melt-rock interaction

818   (Mikuni et al., 2022), and they have erupted at ~0–3 Ma.

819

820 **7 Conclusion**

821

822   The occurrence of petit-spot volcanism supports partial melting at the LAB, providing crucial

823 implications for the nature of this geophysical discontinuity. Multiple petit-spot magmatisms on the

824 western Pacific Plate occurred at ~0–3 Ma, originating from similar PREMA-like melting sources

825 based on $^{40}Ar/^{39}Ar$ dating and the Sr, Nd, and Pb isotopic compositions. The mass balance-based open-

826 system modeling for trace elements revealed that the western Pacific petit-spot magma was generated

827 by the partial melting of a small amount (5%) of oceanic crust-bearing garnet lherzolite with 3–10%

828 carbonatite influx to a given mass of the source. The Sr, Nd, and Pb isotopic compositions of this study

829 samples, with those of the NW Pacific petit-spots, off the Tonga and Java Trenches, could be explained

830 by mixing the EM-1-like and HIMU-like components, which contribute to subducted

831 carbonated/crustal materials. The tectonic-induced magmatism, like a petit-spot, may have the same

832 melting mechanism.

833

834 **Authorship contributions**

835

836   K. Mikuni and N. Hirano conceived the project and performed all experiments. S. Machida and

837 Y. Kato contributed the Sr, Nd, and Pb isotopic analysis using TIMS and MC-ICP-MS. H. Sumino

838 contributed the $^{40}Ar/^{39}Ar$ dating. N. Akizawa, A. Tamura, and T. Morishita helped and performed

EPMA and LA-ICP-MS analyses. S. Machida and N. Hirano conducted the research cruises to gain the rock samples. All authors interpreted the data and wrote the manuscript with comments and improvements.

Competing Interest

The authors declare that they have no conflict of interest.

Data availability

The data newly analyzed in this study and results of geochemical modeling are included in digital format in the online data repository of this paper (Tables 1, 2, 3 and 4, and Supplementary Tables S1 to S6) and the EarthChem online database (DOI will be obtained when it is accepted).

Acknowledgement

We would like to thank the captains, crews, and shipboard scientific parties of the R/V *Yokosuka* and the operating team of the submersible *Shinkai* 6500 for their great work during the YK16-01, YK18-08, and YK19-05S cruises. The Kyoto University Research Reactor Institute is greatfully acknowledged in their assistance of undertaking the radiometric dating. We would like to express our great appreciation to Prof. T. Tsujimori (ORCiD: 0000-0001-9202-7312) for his effort in management of the laboratory at Tohoku University. We also thank R. Fukushima (ORCiD: 0000-0003-2683-6757) for improving the wording in the manuscript. We are really grateful Y. Matamura, Y. Shimbo, and Y. Jindo for their help and discussion on scientific matters. The authors would like to thank Enago (www.enago.jp) for the English language review. This research was supported by the Cooperative Program (No. 106, 202) of Atmosphere and Ocean Research Institute, The University of Tokyo. The Japan Society for the Promotion of Science (Grant Numbers 17K05715, 18H03733, 20K04098) also supported this research.

References

Aftabuzzaman, M.R., Yomogoda, K., Suzuki, S., Takayanagi, H., Ishigaki, A., Machida, S., Asahara, Y., Yamamoto, K., Hirano, N., Sano, S.-I., Chiyonobu, S., Bassi, D. and Iryu, Y.: Multi-approach characterization of shallow-water carbonates off Minamitorishima and their depositional settings/history, Island Arc, 30, e12400, https://doi.org/10.1111/iar.12400, 2021.

Akizawa, N., Ozawa, K., Tamura, A., Michibayashi, K. and Arai, S.: Three-dimensional evolution of melting, heat and melt transfer in ascending mantle beneath a fast-spreading ridge segment

876   constrained by trace elements in clinopyroxene from concordant dunites and host

877   harzburgites of the Oman ophiolite, J. Petrol., 57, 777–814,

878   https://doi.org/10.1093/petrology/egw020, 2016.

879 Akizawa, N., Ohara, Y., Okino, K., Ishizuka, O., Yamashita, H., Machida, S., Sanfilippo, A., Basch,

880   V., Snow, J.E., Sen, A., Hirauchi, K.-I., Michibayashi, K., Harigane, Y., Fujii, M., Asanuma,

881   H. and Hirata, T.: Geochemical characteristics of back-arc basin lower crust and upper

882   mantle at final spreading stage of Shikoku Basin: an example of Mado Megamullion, Prog.

883   Earth Planet. Sci., 8, 65, https://doi.org/10.1186/s40645-021-00454-3, 2021.

884 Akizawa, N., Hirano, N., Matsuzaki, K.M., Machida, S., Tamura, C., Kaneko, J., Iwano, H.,

885   Danhara, T. and Hirata, T.: A direct evidence for disturbance of whole sediment layer in the

886   subducting Pacific plate by petit-spot magma–water/sediment interaction, Mar. Geol., 444,

887   106712, https://doi.org/10.1016/j.margeo.2021.106712, 2022.

888 Asimow, P. D. and Langmuir, C. H.: The importance of water to oceanic mantle melting regimes,

889   Nature, 421, 815–820, https://doi.org/10.1038/nature01429, 2003.

890 Audhkhasi, P. and Singh, S.C.: Discovery of distinct lithosphere-asthenosphere boundary and the

891   Gutenberg discontinuity in the Atlantic Ocean, Sci. Adv., 8, eabn5404,

892   https://doi.org/10.1126/sciadv.abn5404, 2022.

893 Axen G.J., van Wijk, J.W. and Currie, C.A.: Basal continental mantle lithosphere displaced by flat-

894   slab subduction, Nat. Geosci., 11, 961–964, https://doi.org/10.1038/s41561-018-0263-9,

895   2018.

896 Azami, K., Machida, S., Hirano, N., Nakamura, K., Yasukawa, K., Kogiso, T., Nakanishi, M. and

897   Kato, Y.: Hydrothermal ferromanganese oxides around a petit-spot volcano on old and cold

898   oceanic crust, Commun. Earth Environ., 4, 191, https://doi.org/10.1038/s43247-023-00832-

899   3, 2023.

900 Bell, K. and Tilton, G. R.: Probing the mantle: the story from carbonatites, Eos, 83, 273–277,

901   https://doi.org/10.1029/2002EO000190, 2002.

902 Bellas, A., Zhong, S. and Watts, A.B.: Reconciling lithospheric rheology between laboratory

903   experiments, field observations and different tectonic settings, Geophys. J. Int., 228, 857–

904   875, https://doi.org/10.1093/gji/ggab382, 2022.

905 Bianco, T.A, Ito, G., Becker, J.M. and Garcia, M.O.: Secondary Hawaiian volcanism formed by

906   flexural arch decompression, Geochem. Geophys. Geosyst. 6, Q08009,

907   https://doi.org/10.1029/2005GC000945, 2005.

908 Bizimis, M., Salters, V.J.M. and Dawson, J.B.: The brevity of carbonatite sources in the mantle:

909   evidence from Hf isotopes, Contrib. to Mineral. Petrol., 145, 281–300,

910   https://doi.org/0.1007/s00410-003-0452-3, 2003.

911 Bizimis, M., Salters, V.J.M., Garcia, M.O. and Norman, M.D.: The composition and distribution of

the rejuvenated component across the Hawaiian plume: Hf-Nd-Sr-Pb isotope systematics of Kaula lavas and pyroxenite xenoliths, Geochem. Geophys. Geosyst. 14, 4458–4478, https://doi.org/10.1002/ggge.20250, 2013.

Borsova, A.Y. and Tilhac, R.: Derivation of Hawaiian rejuvenated magmas from deep carbonated mantle sources: A review of experimental and natural constraints, Earth. Sci. Rev., 222, 103819, https://doi.org/10.1016/j.earscirev.2021.103819, 2021.

Buchs, D.M., Pilet, S., Cosca, M., Flores, K.E., Bandini, A.N. and Baumgartner, P.O.: Low-volume intraplate volcanism in the Early/Middle Jurassic Pacific basin documented by accreted sequences in Costa Rica, Geochem. Geophys. Geosyst.,14, 1552–1568, https://doi.org/10.1002/ggge.20084, 2013.

Chantel, J., Manthilake, G., Andrault, D., Novella, D., yu, T. and Wang, Y.: Experimental evidence supports mantle partial melting in the asthenosphere, Sci. Adv., 2, e1600246, https://doi.org/10.1126/sciadv.1600246, 2016.

Chen, X., Wang, M., Inoue, T., Liu, Q., Zhang, L. and Bader, T.: Melting of carbonated pelite at 5.5–15.5 GPa: implications for the origin of alkali-rich carbonatites and the deep water and carbon cycles, Contrib. to Mineral. Petrol., 177, 2, https://doi.org/10.1007/s00410-021-01867-5, 2022.

Clague, D.A. and Frey, F.A.: Petrology and Trace element Geochemistry of the Honolulu Volcanics, Oahu: Implications for the Oceanic Mantle below Hawaii, J, Petrol., 23, 447–504, https://doi.org/10.1093/petrology/23.3.447, 1982.

Clague, D.A., Holcomb, R.T., Sinton, J.M., Detrick, R.S. and Torresan, M.E.: Pliocene and Pleistocene alkali flood basalts on the seafloor north of the Hawaiian island, Earth Planet. Sci. Lett., 98, 175–191, https://doi.org/10.1016/0012-821X(90)90058-6, 1990.

Clague, D.A., Moore, J.G.: The proximal part of the giant submarine Wailau landslide, Molokai, Hawaii, J. Volcanol. Geotherm. Res., 113, 259–287, https://doi.org/10.1016/S0377-0273(01)00261-X, 2002.

Collerson, K.D., Williams, Q., Ewart, A.E. and Murphy, D.T.: Origin of HIMU and EM-1 domains sampled by ocean island basalts, kimberlites and carbonatites: The role of CO2-fluxed lower mantle melting in thermochemical upwellings, Phys. Earth Planet. Inter., 181, 112–131, https://doi.org/10.1016/j.pepi.2010.05.008, 2010.

Conrad, C.P., Bianco, T.A., Smith, E.I. and Wessel, P.: Patterns of intraplate volcanism controlled by asthenospheric shear. Nat. Geosci., 4, 317–321, https://doi.org/10.1038/ngeo1111, 2011.

Cousens, B.L. and Clague, D.A.: Shield to Rejuvenated Stage Volcanism on Kauai and Niihau, Hawaiian Islands, J. Petrol., 56, 1547–1584, https://doi.org/10.1093/petrology/egv045, 2015.

Dasgupta, R. and Hirschmann, M.M.: Melting in the Earth's deep upper mantle caused by carbon

948   dioxide, Nature, 440, 659–662, https://doi.org/10.1038/nature04612, 2006.

949   Dasgupta, R., Hirschmann, M.M. and Stalker, K.: Immiscible Transition from Carbonate-rich to

950   Silicate-rich Melts in the 3 GPa Melting Interval of Eclogite + CO2 and Genesis of Silica-

951   undersaturated Ocean Island Lavas, J. Petrol., 47, 647–671,

952   https://doi.org/10.1093/petrology/egi088, 2006.

953   Dasgupta, R., Hirschmann, M.M. and Smith, N.D.: Partial Melting Experiments of Peridotite + CO2

954   at 3 GPa and Genesis of Alkalic Ocean Island Basalts, J. Petrol., 48, 2093–2124,

955   https://doi.org/10.1093/petrology/egm053, 2007.

956   Dasgupta, R., Hirschmann, M.M., McDonough, W.F., Spiegelman, M. and Withers, A.: Trace

957   element partitioning between garnet lherzolite and carbonatite at 6.6 and 8.6 GPa with

958   applications to the geochemistry of the mantle and of mantle-derived melts, Chem. Geol.,

959   262, 57–77, https://doi.org/10.1016/j.chemgeo.2009.02.004, 2009.

960   Dasgupta, R., Mallik, A., Tsuno, K., Withers, A.C., Hirth, G. and Hirschmann, M.M.: Carbon-

961   dioxide-rich silicate melt in the Earth's upper mantle, Nature, 493, 211–215,

962   https://doi.org/10.1038/nature11731, 2013.

963   Debayle, E., Bodin, T., Durand, S. and Ricard, Y.: Seismic evidence for partial melt below tectonic

964   plates, Nature, 586, 555–559, https://doi.org/10.1038/s41586-020-2809-4, 2020.

965   Dixon, J., Clague, D.A., Cousens, B., Monsalve, M.L. and Uhl, J.: Carbonatite and silicate melt

966   metasomatism of the mantle surrounding the Hawaiian plume: evidence from volatiles, trace

967   elements, and radiogenic isotopes in rejuvenated-stage lavas from Niihau, Hawaii,

968   Geochem. Geophys. Geosyst., 9, Q09005, https://doi.org/10.1029/2008GC002076, 2008.

969   Ebisawa, N., Sumino, H., Okazaki, R., Takigami, Y., Hirano, N., Nagao, K. and Kaneoka, I.:

970   Construction of I-Xe and ^{40}Ar–^{39}Ar dating system using a modified VG3600 noble gas mass

971   spectrometer and the first I-Xe data obtained in Japan, J. Mass Spectrom. Soc. Jpn., 52,

972   219–229, https://doi.org/10.5702/massspec.52.219, 2004.

973   Falloon, T. J. and Green, D. H.: The solidus of carbonated, fertile peridotite. Earth Planet. Sci. Lett.

974   94, 364–370, https://doi.org/10.1016/0012-821X(89)90153-2, 1989.

975   Falloon, T. J. and Green, D. H.: Solidus of carbonated fertile peridotite under fluid-saturated

976   conditions. Geology, 18, 195–199, https://doi.org/10.1130/0091-

977   7613(1990)018<0195:SOCFPU>2.3.CO;2, 1990.

978   Falloon, T.J. Hoernle, K., Schaefer, B.F., Bindeman, I.N., Hart, S.R., Garbe-Schonberg, D. and

979   Duncan, R.A.: Petrogenesis of Lava from Christmas Island, Northeast Indian Ocean:

980   Implications for the Nature of Recycled Components in Non-Plume Intraplate Settings,

981   Geosci., 12, 118, https://doi.org/10.3390/geosciences12030118, 2022.

982   Frey, F.A., Green, D.H. and Roy, S.D.: Integrated Models of Basalt Petrogenesis: A Study of Quartz

983   Tholeiites to Olivine Melilitites from South Eastern Australia Utilizing Geochemical and

984 Experimental Petrological Data, J. Petrol., 19, 463–513,

985 https://doi.org/10.1093/PETROLOGY/19.3.463, 1978.

986 Frey, F.A., Clague, D., Mahoney, J.J. and Sinton, J.M.: Volcanism at the edge of the Hawaiian

987 plume: Petrogenesis of submarine alkali lavas from the North Arch volcanic field, J. Petrol.,

988 41, 667–691, https://doi.org/10.1093/petrology/41.5.667, 2000.

989 Foley, S. F., Yaxley, G. M., Rosenthal, A., Buhre, S., Kiseeva, E. S., Rapp, R. P. and Jacob, D. E.:

990 The composition of near-solidus melts of peridotite in the presence of CO_2 and H_2O

991 between 40 and 60 kbar. Lithos, 112, 274–283, https://doi.org/10.1016/j.lithos.2009.03.020,

992 2009.

993 Fujie, G., Kodaira, S., Nakamura, Y., Morgan, J.P. Dannowski, A., Thorwart, M., Grevemeyer, I. and

994 Miura, S.: Spatial variations of incoming sediments at the northeastern Japan arc and their

995 implications for megathrust earthquakes, Geology, 48, 614–619,

996 https://doi.org/10.1130/G46757.1, 2020.

997 Fujiwara, T., Hirano, N. Abe, N. and Takizawa, K.: Subsurface structure of the "petit-spot"

998 volcanoes on the northwestern Pacific Plate, Geophys. Res. Lett., 34, L13305,

999 https://doi.org/10.1029/2007GL030439, 2007.

1000 Garcia, M.O., Weis, D., Jicha, B.R., Ito, G. and Hanano, D.: Petrology and geochronology of lavas

1001 from Ka'ula Volcano: Implications for rejuvenated volcanism of the Hawaiian mantle

1002 plume, Geochim. Cosmochim. Acta., 185, 278–301,

1003 https://doi.org/10.1016/j.gca.2016.03.025, 2016.

1004 Ghosh, S., Ohtani, E., Litasov, K.K. and Terasaki, H.: Solidus of carbonated peridotite from 10 to 20

1005 GPa and origin of magnesiocarbonatite melt in the Earth's deep mantle, Chem. Geol., 262,

1006 17–28, https://doi.org/10.1016/j.chemgeo.2008.12.030, 2009.

1007 Grassi, D. and Schmidt, M.W.: The Melting of Carbonated Pelites from 70 to 700 km Depth, J.

1008 Petrol., 52, 765–789, https://doi.org/10.1093/petrology/egr002, 2011.

1009 Gripp, A.E. and Gordon, R.G.: Current plate velocities relative to the hotspots incorporating the

1010 NUVEL-1 global plate motion model, Geophys. Res. Lett., 17, 1109–1112,

1011 https://doi.org/10.1029/GL017i008p01109, 1990.

1012 Hammouda, T., Manthilake, G., Goncalves, P., Chantel, J., Guignard, J., Crichton, W. and Gaillard,

1013 F.: Is There a Global Carbonate Layer in the Oceanic Mantle?, Geophys. Res. Lett., 48,

1014 e2020GL089752, https://doi.org/10.1029/2020GL089752, 2020.

1015 Hanano, D., Scoates, J.S. and Weis, D: Alteration mineralogy and the effect of acid-leaching on the

1016 Pb-isotope systematics of ocean-island basalts, Am. Mineral., 94, 17–26,

1017 https://doi.org/10.2138/am.2009.2845, 2009.

1018 Hanyu, T., Tatsumi, Y., Senda, R., Miyazaki, T., Chang, Q., Hirahara, Y., Takahashi, T., Kawabata,

1019 H., Suzuki, K., Kimura, J-I. and Nakai, S.: Geochemical characteristics and origin of the

HIMU reservoir: A possible mantle plume source in the lower mantle, Geochem. Geophys. Geosyst., 12, Q0AC09, https://doi.org/10.1029/2010GC003252, 2011.

Hanyu, T., Shimizu, K., Ushikubo, T., Kimura, J.-I., Chang, Q., Hamada, M., Ito, M., Iwamori, H. and Ishikawa, T.: Tiny droplets of ocean island basalts unveil Earth's deep chlorine cycle, Nat. Commun., 10, 60, https://doi.org/10.1038/s41467-018-07955-8, 2019.

Hart, S.R.: A large-scale isotope anomaly in the Southern Hemisphere mantle, Nature, 309, 753–757, https://doi.org/10.1038/309753a0, 1984.

Hart, S.R., Gerlach, D.C. and White, W.M.: A Possible new Sr-Nd-Pb mantle array and consequences for mantle mixing, Geochim. Cosmochim. Acta., 50, 1551–1557, https://doi.org/10.1016/0016-7037(86)90329-7, 1986.

Hein, J.R., Koschinsky, A., Bau, M., Manheim, F.T., Kang, J.K. and Roberts, L.: Cobalt-rich ferromanganese crusts in the Pacific, Handbook of Marine Mineral Deposits (Cronan DS, ed.), 239–279, CRC Press, Boca Raton, Florida, 1999.

Helz, R.T. and Thronber, C.R.: Geochemistry if Kilauea Iki lava lake, Hawaii, Bull. Volcanol., 49, 651–658, https://doi.org/10.1007/BF01080357, 1987.

Herath, P., Stern, T.A., Savage, M.K., Bassett, D. and Henrys, S.: Wide-angle seismic reflections reveal a lithosphere-asthenosphere boundary zone in the subducting Pacific Plate, New Zealand, Sci. Adv., 8, eabn5697, https://doi.org/10.1126/sciadv.abn5697, 2022.

Herzberg, C.: Petrology and thermal structure of the Hawaiian plume from Mauna Kea volcano, Nature, 444, 605–609. https://doi.org/10.1038/nature05254, 2006.

Herzberg, C.: Identification of Source Lithology in the Hawaiian and Canary Islands: Implications for Origins, J. Petrol., 52, 113–146, https://doi.org/10.1093/petrology/egq075, 2011.

Hirano, N., Takahashi, E., Yamamoto, J., Abe, N., Ingle, S.P., Kaneoka, I., Hirata, T., Kimura, J.-I., Ishii, T., Ogawa, Y., Machida, S. and Suyehiro, K.: Volcanism in response to plate flexure. Science, 313, 1426–1428. https://doi.org/10.1126/science.1128235, 2006.

Hirano, N.: Petit-spot volcanism: a new type of volcanic zone discovered near a trench, Geochem. J., 45, 157–167, https://doi.org/10.2343/geochemj.1.0111, 2011.

Hirano, N., Machida, S., Abe, N., Morishita, T., Tamura, A. and Arai, S.: Petit-spot lava fields off the central Chile trench induced by plate flexure, Geochem. J., 47, 249–257, https://doi.org/10.2343/geochemj.2.0227, 2013.

Hirano, N., Nakanishi, M., Abe, N. and Machida, S.: Submarine lava fields in French Polynesia, Mar. Geol., 373, 39–48, http://dx.doi.org/10.1016/j.margeo.2016.01.002, 2016.

Hirano, N., Machida, S., Sumino, H., Shimizu, K., Tamura, A., Morishita, T., Iwano, H., Sakata, S., Ishii, T., Arai, S., Yoneda, S., Danhara, T. and Hirata, T.: Petit-spot volcanoes on the oldest portion of the Pacific Plate, Deep Sea Res. Part I, 154, 103142, https://doi.org/10.1016/j.dsr.2019.103142, 2019.

1056   Hirano, N., Sumino, H., Morishita, T., Machida, S., Kawano, T., Yasukawa, K., Hirata, T., Kato, Y.
1057   and Ishii, T.: A Paleogene magmatic overprint on Cretaceous seamounts of the western
1058   Pacific, Island Arc, 30, e12386, https://doi.org/10.1111/iar.12386, 2021.

1059   Hirano, N. and Machida, S.: The mantle structure below petit-spot volcanoes, Commun. Earth
1060   Environ., 3, 110, https://doi.org/10.1038/s43247-022-00438-1, 2022.

1061   Hirth, G. and Kohlstedt, D.L.: Water in the oceanic upper mantle: implications for rheology, melt
1062   extraction and the evolution of the lithosphere. Earth Planet. Sci. Lett., 144, 93–108,
1063   https://doi.org/10.1016/0012-821X(96)00154-9, 1996.

1064   Hoernle, K., Tilton, G., Le Bas, M.J., Duggem, S. and Garbe-Schönberg, D.: Geochemistry of
1065   oceanic carbonatites compared with continental carbonatites: mantle recycling of oceanic
1066   crustal carbonate, Contrib. to Mineral. Petrol., 142, 520–542,
1067   https://doi.org/10.1007/s004100100308, 2002.

1068   Hofmann, A.W.: Mantle geochemistry: the message from oceanic volcanism, Nature, 385, 219–229,
1069   https://doi.org/10.1038/385219a0, 1997.

1070   Hofmann, A.W.: Sampling mantle heterogeneity through oceanic basalts: isotopes and trace
1071   elements. In: Carson, R. W. (Ed.), Treatise on Geochemistry, 2, The Mantle and Core,
1072   Elsevier, 61–101, https://doi.org/10.1016/B0-08-043751-6/02123-X, 2003.

1073   Hosseini, K., Matthews, K.J., Sigloch, K., Shephard, G.E., Domeier, M. and Tsekhmistrenko, M.:
1074   SubMachine: Web-Based tools for exploring seismic tomography and other models of
1075   Earth's deep interior, Geochem. Geophys. Geosyst., 19, 1464–1483,
1076   https://doi.org/10.1029/2018GC007431, 2018.

1077   Hua, J., Fisher, K. M., Becker, T.W., Gazel, E. and Hirth, G.: Asthenospheric low-velocity zone
1078   consistent with globally prevalent partial melting, Nat. Geosci., 16, 175–181,
1079   https://doi.org/10.1038/s41561-022-01116-9, 2023.

1080   Hulett, S.R., Simonetti, A., Rasbury, E.T. and Hemming, N.G.: Recycling of subducted crustal
1081   components into carbonatite melts revealed by boron isotopes, Nat. Geosci., 9, 904–908,
1082   https://doi.org/10.1038/ngeo2831, 2016.

1083   Irvine, T. N. and Baragar, W. R. A.: A Guide to the Chemical Classification of the Common Volcanic
1084   Rocks, Can. J. Earth Sci., 8, 523–548, https://doi.org/10.1139/e71-055, 1971.

1085   Irving, A.J and Green, D.H.: Geochemistry and petrogenesis of the newer basalts of Victoria and
1086   South Australia, J. Geol. Sci. Australia., 23, 45–66,
1087   https://doi.org/10.1080/00167617608728920, 1976.

1088   Iwata, N.: Geochronological study of the Deccan volcanism by the $^{40}Ar–^{39}Ar$ method, Doctor
1089   Thesis, University of Tokyo, pp. 168, 1998.

1090   Jochum, K.P. and Nohl, U.: Reference materials in geochemistry and environmental research and the

GeoReM database, Chem. Geol., 253, 50–53,

https://doi.org/10.1016/j.chemgeo.2008.04.002, 2008.

Johnson, K.T.M., Dick, H.J.B. and Shimizu, N.: Melting in the oceanic upper mantle: An ion

microprobe study of diopsides in abyssal peridotites, J. Geophys. Res., 95, 2661–2678,

https://doi.org/10.1029/JB095iB03p02661, 1990.

Juriček, M.P and Keppler, H.: Amphibole stability, water storage in the mantle, and the nature of the

lithosphere-asthenosphere boundary, Earth Planet. Sci. Lett., 608, 118082,

https://doi.org/10.1016/j.epsl.2023.118082, 2023.

Kaneko, J., Machida, S., Hirano, N., Kasaya, T. and Kumagai, H.: Near bottom MBES survey

mounted on a HOV at 5500m depth. Oceans Conference Record (IEEE) 2022, 1–5,

https://doi.org/10.1109/OCEANSChennai45887.2022.9775366, 2022.

Kang, L. and Karato, S. -I.: Hydrogen Partitioning Between Olivine and Orthopyroxene:

Implications for the Lithosphere-Asthenosphere Structure, J. Geophys. Res., 128,

e2022JB025259, https://doi.org/10.1029/2022JB025259, 2023.

Karato, S.-I. and Jung, H.: Water, partial melting and the origin of the seismic low velocity and high

attenuation zone in the upper mantle, Earth Planet. Sci. Lett., 157, 193–207,

https://doi.org/10.1016/S0012-821X(98)00034-X, 1998.

Katsura, T. and Fei, H.: Asthenosphere dynamics based on the H_2O dependence of element

diffusivity in olivine, Natl. Sci. Rev., 8, nwaa278. https://doi.org/10.1093/nsr/nwaa278,

2021.

Kawakatsu, H., Kumar, P., Takei, Y., Shinohara, M., Kanazawa, T., Araki, E. and Suyehiro, K.:

Seismic Evidence for Sharp Lithosphere-Asthenosphere Boundaries of Oceanic Plates,

Science, 324, 499–502, https://www.science.org/doi/10.1126/science.1169499, 2009.

Kelemen, P.B., Yogodzinskim G.M., and Scholl, D.W.: Along-strike variation in the Aleutian Island

Arc: genesis of high Mg# andesite and implications for continental crust, In: Eiler, J. (ed.),

Inside the subduction Factory, American Geophysical Union, Geophysical Monograph, 138,

223–276, https://doi.org/10.1029/138GM11, 2003.

Keshav, S. and Gudfinnsson, G.H.: Silicate liquid-carbonatite liquid transition along the melting curve

of model, vapor-saturated peridotite in the system $CaO-MgO-Al_2O_3-SiO_2-CO_2$ from 1.1 to

2 GPa, J. Geophys. Res., 118, 3341–3353, https://doi.org/10.1002/jgrb.50249, 2013.

Kiseeva, E.S., Litasov, K.D., Yaxley, G.M., Ohtani, E. and Kamenetsky, V.S.: Melting and Phase

Relations of Carbonated Eclogite at 9–21 GPa and the Petrogenesis of Alkali-Rich Melts in

the Deep Mantle, J. Petrol., 54, 1555–1583, https://doi.org/10.1093/petrology/egt023, 2013.

Kobayashi, M., Sumino, H., Saito, T., Nagao, K.: Determination of halogens in geological reference

materials using neutron irradiation noble gas mass spectrometry, Chem. Geol., 582, 120420,

https://doi.org/10.1016/j.chemgeo.2021.120420, 2021.

1127   Konovalov, Y. I. and Martynov, Y. A.: Volcanic complex of the La Mont Guyot; Marcus-Wake Uplift,
1128   Pacific Ocean, Pacific Geology, 5, 40–47, 1992.

1129   Konter, J.G., Hanan, B.B., Blicher-Toft, J., Koppers, A.A.P., Plank, T. and Staudigel, H.: One
1130   hundred million years of mantle geochemical history suggest the retiring of mantle plumes
1131   is premature, Earth Planet Sci Lett, 275, 285–295,
1132   https://doi.org/10.1016/j.epsl.2008.08.023, 2008.

1133   Koppers, A. A. P., H. Staudigel. and J. R. Wijbrans.: Dating crystalline groundmass separates of
1134   altered Cretaceous seamount basalts by the Ar^{40}/Ar^{39} incremental heating technique, Chem.
1135   Geol., 166, 139–158. https://doi.org/10.1016/S0009-2541(99)00188-6, 2000.

1136   Koppers, A.A.P., Staudigel, H., Pringle, M.S. and Wijbrans, J.R.: Short-lived and discontinuous
1137   intra-plate volcanism in the South Pacific: hotspots or extensional volcanism?, Geochem.
1138   Geophys. Geosyst., 4, 1089, https://doi.org/10.1029/2003GC000533, 2003.

1139   Korenaga, J.: Plate tectonics and surface environment: Role of the oceanic upper mantle, Earth Sci.
1140   Rev., 205, 103185, https://doi.org/10.1016/j.earscirev.2020.103185, 2020.

1141   Le Bas, M. J., Le Maitre, R., Strackeisen, A. and Zanettin, B. (1986) A chemical classification of
1142   volcanic rocks based on the total alkali–silica diagram, J. Petrol., 27, 745–750,
1143   https://doi.org/10.1093/petrology/27.3.745, 2020.

1144   Lu, C., Grand, S. P., Lai, H. and Garnero, E. J.: TX2019slab: A New P and S Tomography Model
1145   Incorporating Subducting Slabs, J. Geophys. Res., 124, 11549–11567,
1146   https://doi.org/10.1029/2019JB017448, 2019.

1147   Liu, J., Hirano, N., Machida, S., Xia, Q., Tao, C., Liao, S., Liang, J., Li W., Yang, W. Zhang, G. and
1148   Ding, T.: Melting of recycled ancient crust responsible for the Gutenberg discontinuity, Nat.
1149   Commun., 11, 172, https://doi.org/10.1038/s41467-019-13958-w, 2020.

1150   Longerich, H.P., Jackson, S.E. and Gunther, D.: Laser ablation inductively coupled plasma mass
1151   spectrometric transient signal data acquisition and analyte concentration calculation, J. Anal.
1152   At. Spectrom., 11, 899–904, https://doi.org/10.1039/ja9961100899, 1996.

1153   Machida, S., Hirano, N., and Kimura, J.-I.: Evidence for recycled material in Pacific upper mantle
1154   unrelated to plumes, Geochim. Cosmochim. Acta., 73, 3028–3037,
1155   http://dx.doi.org/10.1016/j.gca.2009.01.026, 2009.

1156   Machida, S., Orihashi, Y., Magnani, M., Neo, N., Wilson, S., Tanimizu, M., Yoneda, S., Yasuda, A.
1157   and Tamaki, K.: Regional mantle heterogeneity regulates melt production along the Réunion
1158   hotspot-influenced Central Indian Ridge, Geochem. J., 48, 433–449,
1159   https://doi.org/10.2343/geochemj.2.0320, 2014.

1160   Machida, S., Hirano, N., Sumino, H., Hirata, T., Yoneda, S. and Kato, Y: Petit-spot geology reveals
1161   melts in upper-most asthenosphere dragged by lithosphere, Earth Planet. Sci. Lett., 426,
1162   267–279, https://doi.org/10.1016/j.epsl.2015.06.018, 2015

1163 Machida, S., Fujinaga, K., Ishii, T., Nakamura, K., Hirano, N. and Kato, Y.: Geology and
1164   geochemistry of ferromanganese nodules in the Japanese Exclusive Economic Zone around
1165   Minamitorishima Island, Geochem. J., 50, 539–555,
1166   https://doi.org/10.2343/geochemj.2.0419, 2016.

1167 Machida, S., Kogiso, T. and Hirano, N.: Petit-spot as definitive evidence for partial melting in the
1168   asthenosphere caused by CO_2, Nat. Commun., 8, 14302,
1169   https://doi.org/10.1038/ncomms14302, 2017.

1170 Massuyeau, M., Gardés, E., Morizet, Y. and Gaillard, F.: A model for the activity of silica along the
1171   carbonatite–kimberlite–mellilitite–basanite melt compositional joint, Chem. Geol., 418,
1172   206–216, https://doi.org/10.1016/j.chemgeo.2015.07.025, 2015.

1173 Massuyeau, M., Gardés, E., Rogerie, G., Aulbach, S., Tappe, S., Le Trong, E., Sifré, D. and Gaillaer,
1174   F.: MAGLAB: A computing platform connecting geophysical signatures to melting
1175   processes in Earth's mantle, Phys. Earth Planet., 314, 106638,
1176   https://doi.org/10.1016/j.pepi.2020.106638, 2021.

1177 McKenzie, D. and O'Nions, R.K.: Partial melt distributions from inversion of rare Earth element
1178   concentrations, J. Petrol., 32, 1021–1091, https://doi.org/10.1093/petrology/32.5.1021,
1179   1991.

1180 McKenzie, D. and O'Nions, R.K.: The Source Regions of Ocean Island Basalts, J. Petrol., 36, 133–
1181   159, https://doi.org/10.1093/petrology/36.1.133, 1995.

1182 Melson, W.G., Thompson, G. and van Andel, T.H.: Volcanism and metamorphism in the Mid-
1183   Atlantic Ridge, 22°N latitude, J. Geophys. Res., 73, 5925–5941,
1184   https://doi.org/10.1029/JB073i018p05925, 1968.

1185 Mierdel, K., Keppler, H., Smyth, J.R. and Langenhorst, F.: Water solubility in aluminous
1186   orthopyroxene and the origin of Earth's Asthenosphere, Science, 315, 364–368,
1187   https://doi.org/10.1126/science.1135422, 2007.

1188 Mikuni, K., Hirano, N., Akizawa, N., Yamamoto, J., Machida, S., Tamura, A., Hagiwara, Y.,
1189   Morishita, T.: Lithological structure of western Pacific lithosphere reconstructed from
1190   mantle xenoliths in a petit-spot volcano, Prog. Earth Planet. Sci., 9, 62,
1191   https://doi.org/10.1186/s40645-022-00518-y, 2022.

1192 Miyashiro, A., Shido, F. and Ewing, M.: Metamorphism on the Mid-Atlantic Ridge near 24 and 30°
1193   N. Phil. Trans. Roy. Soc. Lond., 268, 589–603, https://doi.org/10.1098/rsta.1971.0014,
1194   1971.

1195 Morimoto, N.: Nomenclature of pyroxenes. Mineral. Petrol., 39, 55–76,
1196   https://doi.org/10.1007/BF01226262, 1988.

1197 Moore, J.G., Fornari, D.J. and Clague, D.A.: Basalts from the 1877 Submarine Eruption of Mauna
1198   Loa, Hawaii; New Data on the Variation of Palagonitization Rate with Temperature. United

States Geol. Surv. Bull. 1663., 1–11, https://doi.org/10.3133/b1663, 1985.

Müller, R.D., Sdrolias, M., Gaina, C. and Roest, W.R.: Age, spreading rates, and spreading asymmetry of the world's ocean crust. Geochem. Geophys. Geosyst., 9, Q04006. http://dx.doi.org/10.1029/2007GC001743, 2008.

Natland, J.: Petrology of Volcanic Rocks Dredged from Seamounts in the Line Islands, Init. Rep. Deep Sea Drill. Proj., 33, 749–777. https://doi.org/10.2973/dsdp.proc.33.126.1976, 1976.

Nier, A.: A redetermination of the relative abundances of the isotopes of carbon, nitrogen, oxygen, argon, and potassium, Phys. Rev., 77, 789-793, https://doi.org/10.1103/PhysRev.77.789, 1950.

Nobre Silva, I.G., Weis, D., Barling, J. and Scoates, J.S.: Leaching systematics and matrix elimination for the determination of high-precision Pb isotope compositions of ocean island basalts, Geochem. Geophys. Geosyst., 10, Q08012, https://doi.org/10.1029/2009GC002537, 2009.

Novella, D., Keshav, S., Gudfinnsson, G.H. and Ghosh, S.: Melting phase relations of model carbonated peridotite from 2 to 3 GPa in the system $CaO-MgO-Al_2O_3-SiO_2-CO_2$ and further indication of possible unmixing between carbonatite and silicate liquids, J. Geophys. Res., 119, 2780–2800, https://doi.org/10.1002/2013JB010913, 2014.

Nozaki, T., Tokumaru, A., Takaya, Y., Kato, Y., Suzuki, K. and Urabe, T.: Major and trace element compositions and resource potential of ferromanganese crust at Takuyo Daigo Seamount, northwestern Pacific Ocean, Geochem J, 50, 527–537, https://doi.org/10.2343/geochemj.2.0430, 2016.

Okumura, S. and Hirano, N.: Carbon dioxide emission to earth's surface by deep-sea volcanism, Geology, 41, 1167–1170, https://doi.org/10.1130/G34620.1, 2013.

Orihashi, Y., Maeda, J., Tanaka, R., Zeniya, R. and Niida, K.: Sr and Nd isotopic data for the seven GSJ rock reference samples; JA-1, JB-1a, JB-2, JB-3, JG-1a, JGb-1 and JR-1, Geochem. J., 32, 205–211, https://doi.org/10.2343/geochemj.32.205, 1998.

Ozawa, K.: Mass balance equations for open magmatic systems: Trace element behavior and its application to open system melting in the upper mantle. J. Geophys. Res., 106, 13407–13434, https://doi.org/10.1029/2001JB900001, 2001.

Pearce, N.J.G., Perkins, W.T., Westgate, J.A., Gorton, M.P., Jackson, S.E., Neal, C.R. and Chenery, S.P.: A compilation of new and published major and trace element data for NIST SRM 610 and NIST SRM 612 glass reference materials, Geostand. Newsl., 21, 115–144, https://doi.org/10.1111/j.1751-908X.1997.tb00538.x, 1997.

Pilet, S., Baker, M.B. and Stolper, E.M.: Metasomatized Lithosphere and the Origin of Alkaline Lavas, Science, 320, 916–919, https://doi.org/10.1126/science.1156, 2008.

Pilet, S.: Generation of low-silica alkaline lavas: Petrological constrains, models, and thermal

1235   implications, The Interdisciplinary Earth: A Volume in Honor of Don L. Anderson, Gillian

1236   R. Foulger, Michele Lustrino, Scott D. King. https://doi.org/10.1130/2015.2514(17), 2015.

1237 Pilet, S., Abe, N., Rochat, L., Kaczmarek, M.-A., Hirano, N., Machida, S., Buchs, D.M.,

1238   Baumgarther, P.O. and Müntener, O.: Pre-subduction metasomatic enrichment of the oceanic

1239   lithosphere induced by plate flexure, Nat. Geosci., 9, 898–903,

1240   https://doi.org/10.1038/ngeo2825, 2016.

1241 Regelous, M., Weinzierl, C.G. and Haase, K.M.: Controls on melting at spreading ridges from

1242   correlated abyssal peridotite – mid-ocean ridge basalt compositions, Earth Planet. Sci. Lett.,

1243   449, 1–11. http://dx.doi.org/10.1016/j.epsl.2016.05.017, 2016.

1244 Reinhard, A.A., Jackson, M.G., Blusztajn, J., Koppers, A.A.P., Simms, A.R. and Konter, J.G.: "Petit

1245   Spot" Rejuvenated Volcanism Superimposed on Plume-Derived Samoan Shield Volcanoes:

1246   Evidence From a 645-m Drill Core From Tutuila Island, American Samoa, Geochem.

1247   Geophys. Geosys., 20, 1485–1507, https://doi.org/10.1029/2018GC007985, 2019.

1248 Resing, J.A. and Sansone, F.J.: The chemistry of lava–seawater interactions: the generation of

1249   acidity, Geochim. Cosmochim. Acta., 63, 2183–2198, https://doi.org/10.1016/S0016-

1250   7037(99)00193-3, 1999.

1251 Rohrbach, A., Ballhaus, C., Golla-Schindler, U., Ulmer, P., Kamenetsky, V.S. and Kuzmin, D.V.:

1252   Metal saturation in the upper mantle, Nature, 449, 456–458,

1253   https://doi.org/10.1038/nature06183, 2007.

1254 Rychert, C. A. and Shearer, P. M.: A global view of the lithosphere–asthenosphere boundary,

1255   Science, 324, 495–498, https://www.science.org/doi/10.1126/science.1169754, 2009.

1256 Sakamaki, T., Suzuki, A., Ohtani, E., Terasaki, H., urakawa, S., Katayama, Y., Funakoshi, K.-I.,

1257   Wang, Y. Hernlund, J.H. and Ballmer, M.D.: Ponded melt at the boundary between the

1258   lithosphere and asthenosphere, Nat. Geosci., 6, 1041–1044,

1259   https://doi.org/10.1038/ngeo1982, 2013.

1260 Shaw, D.M.: Trace element fractionation during anataxis, Geochim. Cosmochim. Acta., 34, 237–

1261   243, https://doi.org/10.1016/0016-7037(70)90009-8, 1970.

1262 Shaw, C.S.J.: Dissolution of orthopyroxene in basanitic magma between 0.4 and 2 GPa: Further

1263   implications for the origin of Si–rich alkaline glass inclusions in mantle xenoliths, Contrib.

1264   Mineral. Petrol., 135, 114–132, https://doi.org/10.1007/s004100050501, 1999.

1265 Sifré, D., Gardés, E., Massuyeau, M., Hashim, L., Hier-Majumder, S. and Gaillard, F.: Electrical

1266   conductivity during incipient melting in the oceanic low-velocity zone, Nature, 509, 81–85,

1267   https://doi.org/10.1038/nature13245, 2014.

1268 Smith, W.H.F., Staudigel, H., Watts, A.B. and Pringle, M.S.: The Magellan seamounts: early

1269   Cretaceous record of the South Pacific isotopic and thermal anomaly, J. Geophys. Res., 94,

1270   10501–10523, https://doi.org/10.1029/JB094iB08p10501, 1989.

1271   Staudigel, H. and Hart, S.R.: Alteration of basaltic glass: processes and significance for the oceanic
1272   crust-sewater budget, Geochim. Cosmochim. Acta., 47, 337–350,
1273   https://doi.org/10.1016/0016-7037(83)90257-0, 1983.

1274   Staudigel, H., Park, K.H., Pringle, M., Rubenstone, J.L., Smith, W.H.F. and Zindler, A.: The
1275   longevity of the South-Pacific isotopic and thermal anomaly, Earth Planet. Sci. Lett., 102,
1276   24–44, https://doi.org/10.1016/0012-821X(91)90015-A, 1991.

1277   Stixrude, L. and Lithgow-Bertelloni, C.: Thermodynamics of mantle minerals — I. Physical
1278   properties, Geophys. J. Int., 162, 610–632, https://doi.org/10.1111/j.1365-
1279   246X.2005.02642.x, 2005.

1280   Stoenner, R.W., Schaeffer, O.A. and Katcoff, S.: Half-lives of argon-37, argon-39, and argon-42,
1281   Science, 148, 1325–1328, https://doi.org/10.1126/science.148.3675.1325, 1965.

1282   Stracke A., Michael, W., Felix, G., Paul, B. and Erin, T.: Major and trace element concentrations and
1283   Sr, Nd, Hf, Pb isotope ratios of global mid ocean ridge and ocean island basalts, GRO data,
1284   V1, https://doi.org/10.25625/0SVW6S, 2022.

1285   Sun, S.-S. and McDonough, W.F.: Chemical and isotopic systematics of oceanic basalts: implications
1286   for mantle composition and processes, Geol. Soc. Spec. Publ., 42, 313–345,
1287   https://doi.org/10.1144/GSL.SP.1989.042.01.19, 1989.

1288   Takahashi, E.: Origin of basaltic magmas: Implications from peridotite melting experiments and an
1289   olivine fractionation model (in Japanese with English abstract), Bull. Volcanol. Soc. Jpn.,
1290   2nd Ser, 30, S17–S40, https://doi.org/10.18940/kazanc.30.TOKUBE_S17, 1986.

1291   Takahashi, E., Uto, K. and Schilling, J.-G.: Primary magma compositions and Mg/Fe ratios of their
1292   mantle residues along Mid Atlantic Ridge 29° N to 73°N, Technical Report of ISEI
1293   Okayama University Series A, 9, 1–4, 1987.

1294   Tamura, A., Arai, S., Takeuchi, M., Miura, M. and Pirnia, T.: Compositional heterogeneity of a
1295   websterite xenolith from Kurose, southwest Japan: insights into the evolution of lower crust
1296   beneath the Japan Arc, Eur. J. Mineral., 31, 35–47, https://doi.org/10.1127/ejm/2018/0030-
1297   2803, 2019.

1298   Taneja, R., Rushmer, T., Blichert-Toft, J., Turner, S. and O'Neill, C.: Mantle heterogeneities beneath
1299   the Northeast Indian Ocean as sampled by intra-plate volcanism at Christmas Island, Lithos,
1300   262, 561–575, http://dx.doi.org/10.1016/j.lithos.2016.07.027, 2016.

1301   Tanimizu, M. and Ishikawa, T.: Development of rapid and precise Pb isotope analytical techniques
1302   using MC-ICPMS and new results for GSJ rock reference samples, Geochem. J., 40, 121–
1303   133. https://doi.org/10.2343/geochemj.40.121, 2006.

1304   Tatsumi, Y., Sakuyama, M., Fukuyama, H. and Kushiro, I.: Generation of arc basalt magmas and
1305   thermal structure of the mantle wedge in subduction zones, J. Geophys. Res., 88, 5815–
1306   5825, https://doi.org/10.1029/JB088iB07p05815, 1983.

1307 Tivey, M.A., Sager, W.W., Lee, S.-M. and Tominaga, M.: Origin of the Pacific Jurassic quiet zone,
1308   Geology, 34, 789–792, https://doi.org/10.1130/G22894.1, 2006.

1309 Uenzelmann-Neben, G., Schmidt, D.N., Niessen, F. and Stein, R.: Intraplate volcanism off South
1310   Greenland: caused by glacial rebound?, Geophys. J. Int., 190, 1–7,
1311   https://doi.org/10.1111/j.1365-246X.2012.05468.x, 2012.

1312 Valentine, G.A. and Hirano, N.: Mechanisms of low-flux intraplate volcanic fields—Basin and
1313   Range (North America) and northwest Pacific Ocean, Geology, 38, 55–58,
1314   https://doi.org/10.1130/G30427.1, 2010.

1315 Walter, M.J.: Melting of garnet peridotite and the origin of komatiite and depleted lithosphere, J.
1316   Petrol., 39, 29–60, https://doi.org/10.1093/petroj/39.1.29, 1998.

1317 Wakaki, S., Shibata, S.-N. and Tanaka, T.: Isotope ratio measurements of trace Nd by the total
1318   evaporation normalization (TEN) method in thermal ionization mass spectrometry, Int. J.
1319   Mass Spectrom., 264, 157–163, http://dx.doi.org/10.1016/j.ijms.2007.04.006, 2007.

1320 Wang, D., Mookherjee, M., Xu Y. and Karato, S.-I.: The effect of water on the electrical conductivity
1321   of olivine, Nature, 443, 977–980, https://doi.org/10.1038/nature05256, 2006.

1322 Wang, X.-J., Chen, L.-H., Hofmann, A.W., Hanyu, T., Kawabata, H., Zhong, Y., Xie, L.-W., Shi, J.-
1323   H., Miyazaki, T., Hirata, Y., Takahashi, T., Senda, R., Chang, O., Vaglarov, B.S. and Kimura,
1324   J.-I. Recycled ancient ghost carbonate in the Pitcairn mantle plume, PNAS, 115, 8682–8687,
1325   https://doi.org/10.1073/pnas.1719570115, 2018.

1326 Weis, D. and Frey, F.A.: Isotope geochemistry of the Ninetyeast Ridge basement basalts: Sr, Nd, and
1327   Pb evidence for involvement of the Kerguelen hot spot, Proc. Ocean Drill. Program Sci.
1328   Results, 121, 591–610, 1991.

1329 Weis, D. and Frey, F.A.: Role of the Kerguelen Plume in generating the eastern Indian Ocean
1330   seafloor. J. Geophys. Res., 101, 13381–13849, https://doi.org/10.1029/96JB00410, 1996.

1331 Weis, D., Kieffer, B., Maerschalk, C., Barling, J., de Jong, J., Williams, G.A., Hanano, D., Pretorius,
1332   W., Mattielli, N., Scoates, J.S., Goolaerts, A., Friedman, R. M.and Mahoney, J.B.: High-
1333   precision isotopic characterization of USGS reference materials by TIMS and MC-ICP-MS,
1334   Geochem. Geophys. Geosyst., 7, Q08006, http://dx.doi.org/10.1029/2006GC001283, 2006.

1335 Weiss, Y., Class, C., Goldstein, S.L. and Hanyu, T.: Key new pieces of the HIMU puzzle from
1336   olivines and diamond inclusions, Nature, 537, 666–670,
1337   https://doi.org/10.1038/nature19113, 2016.

1338 Workman, R.K., Hart, S.R., Jackson, M., Regelous, M., Farley, K.A., Blusztajn, J., Kurz, M. and
1339   Staudigel, H.: Recycled metasomatized lithosphere as the origin of the Enriched Mantle II
1340   (EM2) end-member: Evidence from the Samoan Volcanic Chain, Geochem. Geophys.
1341   Geosyst., 5, Q04008, https://doi.org/10.1029/2003GC000623, 2004.

1342 Yamamoto, J., Hirano, N., Abe, N. and Hanyu, T.: Noble gas isotopic compositions of mantle

xenoliths from northwestern Pacific lithosphere, Chem. Geol., 268, 313–323, https://doi.org/10.1016/j.chemgeo.2009.09.009, 2009.

Yamamoto, J., Korenaga, J., Hirano, N. and Kagi, H.: Melt-rich lithosphere-asthenosphere boundary inferred from petit-spot volcanoes, Geology, 42, 967–970, https://doi.org/10.1130/G35944.1, 2014.

Yamamoto, J., Kawano, T., Takahata, N. and Sano, Y.: Noble gas and carbon isotopic compositions of petit-spot lavas from southeast of Marcus Island. Earth Planet. Sci. Lett., 497, 139–148, https://doi.org/10.1016/j.epsl.2018.06.020, 2018.

Yamamoto, J., Hirano, N. and Kurz, M.D.: Noble gas isotopic compositions of seamount lavas from the central Chile trench: Implications for petit-spot volcanism and the lithosphere asthenosphere boundary, Earth Planet. Sci. Lett., 552, 116611, https://doi.org/10.1016/j.epsl.2020.116611, 2020.

Yamazaki, S., Neo, N. and Miyashita, S.: Data report: whole–rock major and trace elements and mineral compositions of the sheeted dike–gabbro transition in ODP Hole 1256D, In Teagle, D. A. H., Alt, J. C., Umino, S., Miyashita, S., Banerjee, N. R., Wilson, D. S. and the Expedition 309/312 Scientists (Eds.), Proceedings Integrated Ocean Drilling Program. 309/312: Washington, DC (Integrated Ocean Drilling Program Management International, Inc.) https://doi.org/10.2204/iodp.proc.309312.203.2009, 2009.

Yang, H.-J., Frey, F.A. and Clague, D.A.: Constraints on the Source Components of Lavas Forming the Hawaiian North Arch and Honolulu Volcanics, J. Petrol., 44, 603–627, https://doi.org/10.1093/petrology/44.4.603, 2003.

Yoshino, T., Matsuzaki, T., Yamashita, S. and Katsura T.: Hydrous olivine unable to account for conductivity anomaly at the top of the asthenosphere, Nature, 443, 973–976, https://doi.org/10.1038/nature05223, 2006.

Zakharov, D.O., Tanaka, R., Butterfield, D.A. and Nakamura, E.: A New Insight Into Seawater-Basalt Exchange Reactions Based on Combined $\delta^{18}O$—$\Delta'^{17}O$—$^{87}Sr/^{86}Sr$ Values of Hydrothermal Fluids From the Axial Seamount Volcano, Pacific Ocean. Front. Earth Sci., 9, 691699, https://doi.org/10.3389/feart.2021.691699, 2021.

Zhang, F., Lin, J. and Zhan, W.: Variations in oceanic plate bending along the Mariana trench. Earth Planet. Sci. Lett., 401, 206–214, http://dx.doi.org/10.1016/j.epsl.2014.05.032, 2014.

Zhang, G.L., Chen, L.H., Jackson, M. and Hofmann, A.W.: Evolution of carbonated melt to alkali basalt in the South China Sea, Nat. Geosci., 10, 229–235, https://doi.org/10.1038/ngeo2877, 2017.

Zhang, W., Johnston, S. and Currie, C.A., Kimberlite magmatism induced by west-dipping subduction of the North American plate, Geology, 47, 395–398, https://doi.org/10.1130/G45813.1, 2019.

1379   Zhang, J., Xu, M. and Sun, Z.: Lithospheric flexural modelling of the seaward and trenchward of the
1380   subducting oceanic plates, Int. Geol. Rev., 62, 908–923,
1381   https://doi.org/10.1080/00206814.2018.1550729, 2020.

1382   Zhang, G., Wang, S., Huang, S., Zhan, M. and Yao, J.: CO_2-rich rejuvenated stage lavas on Hawaiian
1383   Islands, Geochem. Geophys. Geosyst., 23, e2022GC010525,
1384   https://doi.org/10.1029/2022GC010525, 2022.

1385   Zhong, Y., Zhang, G.-L., Zhong, L.-F., Chen, L.-H. and Wang, X.-J.: Post-spreading volcanism
1386   triggered by CO_2 along the South China Sea fossil spreading axis, Lithos, 404–405, 106478,
1387   https://doi.org/10.1016/j.lithos.2021.106478, 2021.

1388   Zindler, A. and Hart, S.: Chemical geodynamics, Ann. Rev. Earth Planet. Sci., 14, 493–571,
1389   https://doi.org/10.1146/annurev.ea.14.050186.002425, 1986.